

The multiphase circumgalactic medium in the epoch of reionization: C II and C IV absorbers around [O III] emitters

Downloaded from: https://research.chalmers.se, 2026-11-23 06:59 UTC

Citation for the original published paper (version of record):
Piscitelli, C., D'Odorico, V., Galbiati, M. et al (2026). The multiphase circumgalactic medium in the epoch of reionization: C II and C IV absorbers
around [O III] emitters. Astronomy and Astrophysics, 715.
http://dx.doi.org/10.1051/0004-6361/202662432

N.B. When citing this work, cite the original published paper.

research.chalmers.se offers the possibility of retrieving research publications produced at Chalmers University of Technology. It covers all kind of research output: articles, dissertations, conference papers, reports etc. since 2004. research.chalmers.se is administrated and maintained by Chalmers Library

(article starts on next page)

A&A, 715, A103 (2026)
https://doi.org/10.1051/0004-6361/202662432
© The Authors 2026

Astronomy & Astrophysics

The multiphase circumgalactic medium in the epoch of reionization: C II and C IV absorbers around [O III] emitters

C. Piscitelli[1,2,⋆], V. D'Odorico[2,3], M. Galbiati[2], M. Bischetti[4,2], G. Cupani[2,3], R. Dutta[5], S. Cantalupo[6], S. Di Stefano[1,2], S. T. Guida[7], K. Knudsen[8], C. Mazzucchelli[9], L. Paquereau[8], L. Pentericci[10], R. Rana[8], F. Ricci[11], F. Salvestrini[2], A. Tortosa[12,10], A. Travascio[2], C. Vignali[12,13], and L. Zappacosta[10]

[1] Department of Physics, Astronomy Section, University of Trieste, Via G.B. Tiepolo, 11, I-34143 Trieste, Italy
[2] INAF – Osservatorio Astronomico di Trieste, Via G. B. Tiepolo 11, I-34143 Trieste, Italy
[3] IFPU – Institute for Fundamental Physics of the Universe, Via Beirut 2, I-34151 Trieste, Italy
[4] Dipartimento di Fisica "Enrico Fermi", Università di Pisa, Largo Bruno Pontecorvo 3, Pisa I-56127, Italy
[5] IUCAA, Postbag 4, Ganeshkhind, Pune 411007, India
[6] Department of Physics, Università degli Studi di Milano-Bicocca, I-20126 Milano, Italy
[7] Max-Planck-Institut für Extraterrestrische Physik (MPE), Giessenbachstrasse 1, 85748 Garching bei München, Germany
[8] Department of Physics and Astronomy, Chalmers University of Technology, SE-412 96 Gothenburg, Sweden
[9] Instituto de Estudios Astrofísicos, Facultad de Ingeniería y Ciencias, Universidad Diego Portales, Avenida Ejército Libertador 441, Santiago, Chile
[10] INAF – Osservatorio Astronomico di Roma, Via Frascati 33, I-00078 Monte Porzio Catone, Italy
[11] Department of Mathematics and Physics, Roma Tre University, Via della Vasca Navale 84, Rome 00146, Italy
[12] INAF – Osservatorio di Astrofisica e Scienza dello Spazio di Bologna, Via Gobetti, 93/3, I-40129 Bologna, Italy
[13] Department of Physics and Astronomy (DIFA), University of Bologna, Via Gobetti, 93/2, I-40129 Bologna, Italy

Received 5 August 2026 / Accepted 16 September 2026

ABSTRACT

We investigate the multiphase circumgalactic medium during the epoch of reionization ($z > 6$) by cross-correlating cool- C II and warm-ionized C IV absorption systems with star-forming [O III] emitters. JWST/NIRCam wide-field slitless spectroscopy from the EIGER survey was combined with medium- and high-resolution optical and NIR spectra of six background quasars, including new VLT/X-Shooter observations of PSO J159-02. We analyzed the relation between 16 C II and 14 C IV absorbers ($\log(N) > 13.0$) and 136 galaxies within an impact parameter of $R_\perp \leq 1000$ pkpc and a line-of-sight separation of $\Delta v \leq 500\,\mathrm{km\,s^{-1}}$. We detected a statistically significant excess of both ions around galaxies compared to a randomized background. The C IV covering fraction remains enhanced up to ∼1 pMpc, whereas C II drops to the background level beyond ∼0.5 pMpc, demonstrating that the warm-ionized phase is more spatially extended than cooler gas. Jointly, the 3D galaxy-absorber spatial clustering is significantly weaker than the galaxy-galaxy autocorrelation. This provides direct physical evidence that early carbon enrichment is not confined to the virial radius of massive star-forming systems; rather, a substantial fraction of these metals permeates the diffuse intergalactic medium or is injected by a widespread population of faint undetected dwarf galaxies. Finally, we note a rapid radial decline of the C IV covering fraction compared with lower-redshift samples at $z < 2$ and $z \sim 3$–4, which indicates an evolving circumgalactic medium ionization structure where early metals predominantly reside in lower ionization states. In conclusion, we determine a conservative lower limit for the observed carbon mass of $\mathrm{M_{C\,II+C\,IV}} \geq 2.8 \times 10^6\,M_\odot$ within 300 pkpc.

Key words. galaxies: halos – galaxies: high-redshift – intergalactic medium – quasars: absorption lines – dark ages, reionization, first stars

1. Introduction

The circumgalactic medium (CGM) plays a fundamental role in the evolution of galaxies, where it serves as an interface between galaxies and the intergalactic medium (IGM). The exchange of baryons, metals, and energy is regulated through the accretion of metal-poor gas, outflows from feedback processes occurring inside galaxies, and recycling of metal-enriched material (for a review, see Tumlinson et al. 2017; Péroux & Howk 2020). The interplay between accretion and feedback processes regulates the availability of the fuel needed by galaxies to sustain their star formation (e.g., Dekel et al. 2009), and at the same time, it enriches and shapes the properties of the CGM gas, producing a multiphase medium that spans a wide range of temperatures, densities, kinematic properties, and chemical abundances (e.g., Oppenheimer & Davé 2008; Faucher-Giguère & Oh 2023).

Because the density of the CGM gas is low and thus is faint, CGM gas is commonly studied in absorption, through the line features it imprints on the spectra of background bright sources, such as quasars.

However, the combination of deep galaxy surveys and high-resolution quasar spectroscopy has allowed us to characterize the CGM at $z \lesssim 4$ (e.g., Adelberger et al. 2005; Steidel et al. 2010; Rudie et al. 2012; Turner et al. 2014; Fumagalli et al. 2015; Burchett et al. 2016; Chen et al. 2017; Rudie et al. 2019; Dutta et al. 2020, 2021; Schroetter et al. 2021; Galbiati et al. 2023; Banerjee et al. 2023; Galbiati et al. 2024; Banerjee et al. 2025, 2026) primarily through metal-doublet transitions, such as Mg II $\lambda\lambda$ 2798, 2803 Å and C IV $\lambda\lambda$ 1548, 1550 Å, which are per-

⋆ Corresponding author: christian.piscitelli@inaf.it

Open Access article, published by EDP Sciences, under the terms of the Creative Commons Attribution License (https://creativecommons.org/licenses/by/4.0), which permits unrestricted use, distribution, and reproduction in any medium, provided the original work is properly cited.
This article is published in open access under the Subscribe to Open model. Subscribe to A&A to support open access publication.

fectly suited to probe different gas phases ranging from the cool ($T \sim 10^4$ K) gas to a more ionized and sometimes warmer phase ($T \sim 10^5$ K). Observations and results from simulations (e.g., Ford et al. 2013; Ho et al. 2021; Weng et al. 2024) revealed that the presence and column density of neutral hydrogen and metal-absorbing gas is strongly correlated statistically with the distance from the galaxies and from the environment. Additionally, Dutta et al. (2021) and Galbiati et al. (2023) have shown that galaxy groups are richer in enriched gas than isolated galaxies. Furthermore, low-ionization ions (e.g., Mg II, C II, and O I) are mostly concentrated closer to the galaxies than higher-ionization ions (e.g., C IV, Si IV, and O IV), which can be detected even up to several times the virial galaxy radii (e.g., Schroetter et al. 2021; Qu et al. 2023).

Analogous investigations in the very high-redshift Universe ($z \gtrsim 5$) are still rare and based on single fields (e.g., Díaz et al. 2021), particularly during the epoch of reionization (EoR; $z > 6$), when the most massive structures were in the early stages of assembly, and the interplay between galaxies and their surrounding gas and nearby galaxies was not yet fully established. In this regime, environmental interactions may be less developed than in the local Universe. More recently, high-redshift studies based on ground- and space-based near-infrared (NIR) quasar spectroscopy have shown that the early Universe was already chemically enriched, revealing an increase in the number density of low-ionization absorbers and a decline in high-ionization species with increasing redshift (Becker et al. 2019; D'Odorico et al. 2022; Davies et al. 2023a,b; Christensen et al. 2023; Sebastian et al. 2024). At the same time, the *James Webb Space Telescope* (JWST) has opened new frontiers providing deep surveys of galaxies such as the *Emission-Line Galaxies and Intergalactic Gas in the Reionization Epoch* (EIGER, Kashino et al. 2023; Matthee et al. 2023; Kashino et al. 2026) and *A SPectroscopic survey of biased halos in the Reionization Era* (ASPIRE, Wang et al. 2023), both centered on samples of $z \sim 6$ quasars for which spectra were available. Bordoloi et al. (2024) and Higginson et al. (2026) studied the connection between high-redshift [O III] emitters in the EIGER fields and Mg II and O I absorbers, respectively. They found that most of the high-z Mg II absorption is not consistent with being bound to the dark matter halos of the host galaxies, while O I at $z \sim 6$ could primarily trace extended overdensity environments rather than the CGM of individual halos. Zou et al. (2024), using ASPIRE data, characterized the CGM at $z \sim 6$–6.5 by linking metal absorbers to surrounding [O III] emitters, suggesting that their chemical abundance modeling in overdense regions favors a top-heavy initial mass function, hinting at a direct contribution from Population III stars to cosmic gas enrichment at the end of reionization.

We exploit the catalog of [O III] emitters in the EIGER fields (Kashino et al. 2026) and the absorption lines identified in the spectra of the six central quasars to investigate the CGM at $z \sim 6$ through the cross-correlation between galaxies and C II (λ 1334 Å) and C IV absorbers. The use of these two ions allows us to investigate the distribution of gas in two different ionization stages that likely trace a colder and hotter medium.

The paper is organized as follows. In Section 2 we describe the galaxy sample from EIGER and the absorption line sample from proprietary and literature data. In Section 3 we study the spatial distribution of C II and C IV absorption around EIGER galaxies. In Section 4 we discuss and compare our results with the low-redshift literature samples, and we present our conclusions in Section 5.

Throughout this work, we adopt a flat ΛCDM cosmology with $H_0 = 70\,\mathrm{km\,s^{-1}\,Mpc^{-1}}$, $\Omega_M = 0.27$, and $\Omega_\Lambda = 0.73$. The uncertainties are computed as 1σ (68.3%) confidence levels. The distances are given in proper units using the prefix p, and the prefix c before the unit refers to the comoving distance.

2. Observational samples

In this section, we describe the properties of galaxies and absorption systems we used for the analysis. Specifically, we first present the catalog of [O III] emitters selected from the EIGER survey, followed by the compilation of C II and C IV absorption systems detected along the background quasar sightlines.

2.1. [O III] emitters

We used the catalog of [O III] emitting galaxies from the EIGER survey provided by Kashino et al. (2026). EIGER is a JWST program (Program ID: 1243; PI: S. J. Lilly) based on *Near-InfraRed Camera* (NIRCam) Wide Field Slitless Spectroscopy (WFSS) of six extragalactic deep fields, each centered on a luminous quasar at $z_{\rm qso} \geq 6.0$. A complete description of the observing program can be found in Kashino et al. (2023), Matthee et al. (2023), Bordoloi et al. (2024). The main properties of the six quasars of the EIGER Survey (hereafter J0148, J1030, J0100, J159, J1148, and J1120) are listed in Table 1. They were selected to have medium- and high-resolution ($R \sim 5000$–$45\,000$) spectra obtained with the Folded-port InfraRed Echellette (FIRE, Simcoe et al. 2008) at the Magellan telescopes, the Multi-Object Spectrometer For Infra-Red Exploration (MOSFIRE, McLean et al. 2010) and the High Resolution Echelle Spectrometer (HIRES, Vogt et al. 1994) at Keck, and X-Shooter (Vernet et al. 2011) at the Very Large Telescope (VLT), amounting to several hundred hours of observations, providing a unique window into the foreground absorbing gas along their line of sight. In addition to these spectroscopic data, the EIGER quasar fields benefit from JWST/NIRCam (Rieke et al. 2023) and *Hubble Space Telescope* (HST) imaging. In particular, the NIRCam F115W, F200W, and F356W filters were used for the JWST imaging.

Galaxies in the EIGER fields are identified as [O III] $\lambda\lambda$ 4960, 5008 Å emitters across the redshift range $z \sim 5.33$–6.97. The [O III] λ 5008 Å fluxes (F_{5008}) were estimated to be within the range $-18 < \log(F_{5008}/[\mathrm{erg\,s^{-1}\,cm^{-2}}]) < -16.5$, and the corresponding luminosities vary from $41.6 < \log(L_{5008}[\mathrm{erg\,s^{-1}}]) < 43.1$ (Kashino et al. 2026). This sample includes star-forming systems spanning a broad range of stellar masses, $6.8 \leq \log(M_\star/M_\odot) \leq 9.3$, and star formation rates averaged over the most recent 50 Myr, $-1 \leq \log(\mathrm{SFR}/M_\odot\,\mathrm{yr^{-1}}) \leq 1.5$ (Higginson et al. 2026). The full sample consists of 948 [O III] emitters (Kashino et al. 2026).

2.2. QSO absorption systems

In order to probe the distribution of gas in the CGM of [O III] emitters, we collected a sample of C II and C IV absorption systems along the lines of sight to the six central quasars.

The sample we used is composed of literature and proprietary data. J0148, J1030 and J0148 belong to the enlarged XQR-30 sample (D'Odorico et al. 2023), for which the catalog of metal absorption lines with measured redshift, column density, and Doppler parameter is provided by Davies et al. (2023a). The absorption systems for J1148 and J1120 are provided by Becker et al. (2006) and Bosman et al. (2017), respectively. However, observations of J1148 were conducted with Keck/HIRES (Vogt et al. 1994), which has a high spectral

Table 1. EIGER sample of quasars.

Quasar name	RA h	Dec deg	z_{em}	Ref	$\Delta z_{\mathrm{C\,II}}$	$\Delta z_{\mathrm{C\,IV}}{}^{a}$
(1)	(2)	(3)	(4)	(5)	(6)	(7)
ULAS J0148+0600	01:48:37.64	+06:00:20.06	5.9895	D'Odorico et al. (2023)	5.367–5.874	5.33–5.874
SDSS J1030+0524	10:30:27.10	+05:24:55.0	6.304	Farina et al. (2019)	5.653–6.183	5.33–6.183
SDSS J0100+2802	01:00:13.02	+28:02:25.8	6.3269	Venemans et al. (2020)	5.674–6.206	5.33–6.206
PSO J159-02	10:36:54.19	−02:32:37.94	6.3809	Decarli et al. (2018)	5.723–6.259	5.33–6.259
SDSS J1148+5251	11:48:16.64	+52:51:50.3	6.4189	Maiolino et al. (2005)	5.758–6.296	5.33–6.296
ULAS J1120+0641	11:20:01.48	+06:41:24.3	7.0848	Venemans et al. (2020)	6.365–6.951	5.348–6.951

Notes. (1) Quasar name. (2–3) RA and Dec (J2000). (4) Quasar redshift based on [C II] emission line. (5) Redshift reference. (6) Redshift window for the detection of C II systems to avoid contamination from the Lyα forest and the quasar proximity zone. (7) Same as (6) but for C IV. [a] The lower bound of the redshift window is set by the lowest redshift to which JWST observations are sensitive, with the exception of J1120, for which it is determined by the Lyα forest limit.

resolution ($R \sim 45\,000$ for a slit width of 0.86″) and a maximum wavelength of 1 μm. This implies that C IV is only detectable in the J1148 spectrum in the redshift range $4.82 \lesssim z \lesssim 5.46$, which overlaps only very little with the redshift range probed by the EIGER [O III] emitters.

Furthermore, we present a new VLT/X-Shooter spectrum for J159 that improves the signal-to-noise ratio (S/N) by a factor of ∼2 compared to previous observations. The final spectrum has S/N ∼ 22 per 10 km s^{-1} bin measured at $\lambda \simeq 1285$ Å rest frame. The details of the data reduction and analysis of the J159 spectrum, including the identification of absorption systems, are reported in Appendices B and C.

Following Davies et al. (2023a), we created absorption systems by merging velocity components closer than 200 km s^{-1}. The total column density of the system was obtained by summing the column densities of the individual components; the corresponding uncertainty on the total logarithmic column density was calculated via standard error propagation. The redshift of the absorption system was determined as the column-density-weighted mean of the redshifts of the individual components as

$$z_{\mathrm{abs}} = \frac{\sum_i z_i N_i}{\sum_i N_i}, \tag{1}$$

and we used the standard error of the weighted mean as the corresponding uncertainty. Finally, to avoid the proximity region of the background quasar, we excluded [O III] emitters and absorption systems located within a velocity separation of 5000 km s^{-1} from the quasar systemic redshift. Accordingly, the maximum redshift considered for each quasar field was calculated as

$$z_{\mathrm{max}} = (1 + z_{\mathrm{qso}}) \sqrt{\frac{1-\beta}{1+\beta}} - 1, \tag{2}$$

where $\beta = v/c$. To prevent contamination from the Lyα forest in the quasar spectra, we established a minimum redshift threshold for [O III] emitters and absorption systems within the same framework, defined as

$$z_{\mathrm{min}} = (1 + z_{\mathrm{qso}}) \left(\frac{\lambda_{\mathrm{Ly}\alpha}}{\lambda_{\mathrm{ion,rest}}} \right) - 1, \tag{3}$$

where $\lambda_{\mathrm{Ly}\alpha}$ is the rest-frame wavelength of the Lyα transition, and $\lambda_{\mathrm{ion,rest}}$ refers to the rest-frame wavelengths of the C II and C IV transitions. The resulting redshift ranges computed for each quasar field are reported in Table 1.

To ensure the reliability of our statistical analysis and to robustly account for varying spectral noise in different sightlines, the sample was limited to systems satisfying the condition $\log(N) + \sigma_{\log(N)} \geq 13.0$, corresponding to a completeness threshold ≳50% in the considered absorption line samples (Bosman et al. 2017; Davies et al. 2023a). Following these selection criteria, our final sample consisted of 16 C II and 14 C IV absorption systems. We list all the C II and C IV absorbers in Table A.1.

3. Analysis of the relation between galaxies and absorbers

We investigated the physical properties and spatial distribution of the CGM traced by C II and C IV absorbers at $z \sim 6$, establishing the line of sight and angular connection between the absorbers and the EIGER galaxy population.

As a first step, we computed the impact parameter $R_\perp$ for every galaxy, measured in physical kiloparsec (pkpc), which is the projected distance to the quasar line of sight, as

$$R_\perp = \theta \cdot D_A(z_{\mathrm{gal}}), \tag{4}$$

where θ is the angular separation on the sky between the galaxy and the quasar sightline, and D_A is the angular diameter distance calculated at the redshift of the galaxy. As a second step, we computed the line-of-sight distance for every absorber-galaxy pair as a velocity offset, measured in km s^{-1}, as

$$\Delta v = c \cdot \frac{(1+z_{\mathrm{abs}})^2 - (1+z_{\mathrm{gal}})^2}{(1+z_{\mathrm{abs}})^2 + (1+z_{\mathrm{gal}})^2}, \tag{5}$$

where c is the speed of light, and z_{abs} and z_{gal} are the redshifts of the absorption system and galaxy, respectively.

In Fig. 1 we plot these quantities with an absorption-centric perspective, that is, centering on each absorber and considering all galaxies with a velocity offset $|\Delta v| \leq 2500$ km s^{-1}, and an impact parameter $R_\perp \leq 1000$ pkpc.

When a single galaxy is associated with multiple absorbers at different redshifts, we defined the association with the smallest velocity offset as the primary and all the others as the secondary. In Fig. 1 the line-of-sight velocity distribution is obtained by including only primary associations to avoid counting galaxies twice. The distribution reveals a prominent excess of galaxies centered at $\Delta v \simeq 0$ km s^{-1}. For these galaxies, 26% for C II and 55% for C IV are enclosed within a velocity difference of $|\Delta v| \leq 500$ km s^{-1} (indicated by the vertical dashed lines).

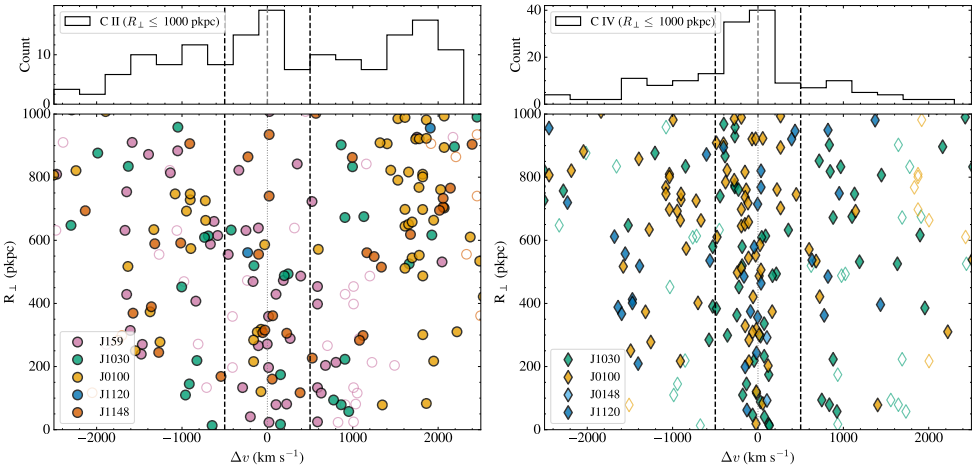

Fig. 1. Projected impact parameter vs. line-of-sight velocity difference between absorbers and galaxies. The left and right panels refer to C II and C IV, respectively. The vertical dashed lines mark the $|\Delta v| \leq 500\,\mathrm{km\,s^{-1}}$ velocity window. The filled circles and diamonds represent primary galaxy associations, while open circles and diamonds denote secondary associations. The different colors indicate the different quasar fields. The upper panels report the distribution of the number of galaxies as a function of the offset velocity.

Based on this result and on previous works (Dutta et al. 2021; Galbiati et al. 2023, 2024), we adopted a velocity threshold of $\pm 500\,\mathrm{km\,s^{-1}}$ to define the association between a galaxy and an absorber. Within this window and an impact parameter of $R_\perp \leq 1$ pMpc, we identified 44 and 92 [O III] emitters around C II and C IV absorbers, respectively (see Table A.1).

Finally, we show in Fig. 2 the 2D distribution of galaxies within $|\Delta v| \leq 500\,\mathrm{km\,s^{-1}}$ of C II and C IV absorbers and impact parameters from the line of sight ≤1000 pkpc.

3.1. Covering fraction

In order to investigate the properties of the CGM around the [O III]-emitting galaxies, we measured the covering fraction of C II and C IV as a function of impact parameter. This quantity is defined as the ratio of the number of [O III] emitters with a C II or C IV absorption system within a velocity offset $|\Delta v_{\max}|$ and the total number of [O III] emitters in the considered impact parameter bin, that is,

$$f_c(R_\perp) = \frac{\sum_{i \in S(R_\perp)} A_i(\Delta v_{\max})}{\sum_{i \in S(R_\perp)} 1}, \tag{6}$$

where $S(R_\perp)$ is the sample of galaxies that fall in the chosen impact parameter bin, while $A_i(\Delta v_{\max})$ is a function that is equal to 1 if there exists an absorber with $|\Delta v| \leq \Delta v_{\max}$ and 0 otherwise. We assumed $|\Delta v_{\max}| = 500\,\mathrm{km\,s^{-1}}$ and impact parameter bins of $\Delta R_\perp = 75$ pkpc up to 375 pkpc, and $\Delta R_\perp = 125$ pkpc between 375 pkpc and 1 pMpc. The uncertainty in the covering fraction was computed by adopting the Wilson-score technique (Wilson 1927; Dean & Pagano 2015), which, unlike the standard normal approximation, is a method that properly accounts for the asymmetry of binomial errors in the small-sample regime, keeping the boundaries strictly confined to [0,1]. The results of this calculation for C II and C IV are reported in Table 2.

To evaluate the significance of the measured covering fractions, we compared them with a background expectation. To this end, we employed a field-shuffling technique. We computed the projected distance and the velocity offsets by cross-matching the absorbers of a given quasar field with the galaxies from all the other five EIGER fields (Kashino et al. 2026), excluding the galaxies from the original field of the absorbers from the iteration. Following this approach, we were able to break any real kinematic or spatial link between gas and galaxies. Then, we computed the covering fractions for the random sample derived from the shuffling, as we did for the original data. The results are shown in Fig. 3 for C II and C IV. The two ions exhibit a significant covering fraction. Specifically, the C II covering fraction remains above 20% up to projected distances of 500 pkpc; at larger separations, it drops to 10% and becomes consistent with the background signal. In contrast, the C IV covering fraction remains significantly enhanced with respect to the background (by a factor of 2 at least) up to the maximum probed separation of ∼1 pMpc because the same C IV absorber can be associated with multiple galaxies at the same redshift and because 12 over 14 C IV absorption systems are associated with groups of galaxies extending to impact parameters beyond 500 pkpc (see Table A.1). To quantify the impact of group multiplicity, we recalculated the C IV covering fraction by matching each absorber only with the galaxy with the smallest impact parameter within the considered velocity window. This restriction caused the extended plateau to completely vanish, with the covering fraction dropping to the random background level beyond $R_\perp \simeq 300$–400 pkpc (see Fig. A.1). This confirms that the extended highly ionized gas signal at large distances is primarily driven by group environments.

It is important to note that the covering fractions for the considered ions are not independent measurements because several systems show C II and C IV at the same redshift. To account for this, we again computed the covering fraction without the C IV covering fraction of the systems with associated low-ionization lines (not just C II but also O I, Si II, Fe II, Al II, Mg II). The result is shown in Fig. A.1, where the enhanced covering fraction in the first bin has disappeared and it has decreased out to ≃400 pkpc; while on the larger scales, the signal is still significantly higher than the background by a factor of 2 at least.

Then, we tested the possible dependence of the covering fraction on the chosen impact parameter bin size. To do this, we varied the bin edges of ±5 pkpc, and using a Monte Carlo (MC) algorithm, we investigated potential variations in the covering fraction trend, particularly for C IV absorbers. We performed 300 iterations, randomly shifting the bin edges within the mentioned range. This test showed that the variations are marginal compared to the 1σ uncertainty of the covering fraction in each interval. This demonstrates that our results are physically driven and not affected by binning artifacts or small-number statistics.

Finally, we computed the cumulative covering fraction. Physically, this quantity represents the average probability that a random sightline passing anywhere within a projected distance $R_\perp$ from a central [O III] emitter intersects gas containing C II or C IV. As we did for the differential covering fraction, we obtained a random background with the shuffling technique

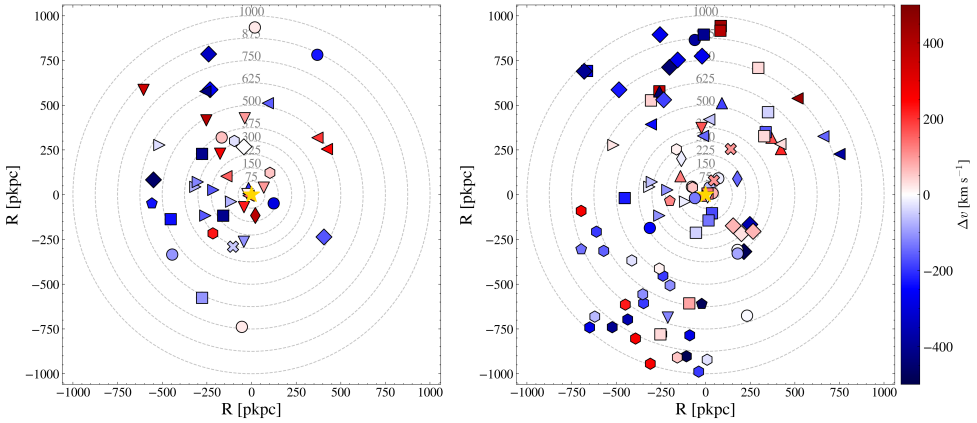

Fig. 2. 2D distribution of galaxies associated with C II (left panel) and C IV (right panel) absorbers. The central gold star indicates the position of the line of sight. The same symbol indicates different galaxies within $|\Delta v| \leq 500\,\mathrm{km\,s^{-1}}$ of the same absorber.

Table 2. Differential covering fraction of C II and C IV absorbers around [O III] emitters evaluated within a velocity window of $|\Delta v| \leq 500\,\mathrm{km\,s^{-1}}$, including the combined C II + C IV differential covering fraction shown in Fig. 8.

$\Delta R_\perp$ pkpc	C II Tot	C II Det	C II f_c	C IV Tot	C IV Det	C IV f_c	C II + C IV Tot	C II + C IV Det	C II + C IV f_c
0–75	6	3	$0.500^{+0.189}_{-0.189}$	10	6	$0.600^{+0.139}_{-0.157}$	6	4	$0.667^{+0.156}_{-0.204}$
75–150	17	5	$0.294^{+0.097}_{-0.119}$	25	7	$0.280^{+0.097}_{-0.080}$	17	9	$0.471^{+0.119}_{-0.116}$
150–225	17	4	$0.235^{+0.086}_{-0.116}$	25	5	$0.200^{+0.091}_{-0.068}$	17	6	$0.294^{+0.119}_{-0.097}$
225–300	20	4	$0.200^{+0.074}_{-0.103}$	31	6	$0.194^{+0.080}_{-0.061}$	20	8	$0.350^{+0.111}_{-0.097}$
300–375	20	7	$0.350^{+0.097}_{-0.111}$	41	9	$0.220^{+0.071}_{-0.058}$	20	9	$0.350^{+0.111}_{-0.097}$
375–500	30	6	$0.200^{+0.063}_{-0.082}$	69	9	$0.130^{+0.046}_{-0.035}$	30	11	$0.367^{+0.091}_{-0.082}$
500–625	46	5	$0.109^{+0.038}_{-0.054}$	71	11	$0.155^{+0.048}_{-0.038}$	46	14	$0.283^{+0.070}_{-0.061}$
625–750	45	4	$0.089^{+0.034}_{-0.052}$	83	11	$0.133^{+0.042}_{-0.033}$	45	10	$0.222^{+0.068}_{-0.056}$
750–875	38	3	$0.079^{+0.034}_{-0.055}$	63	12	$0.190^{+0.054}_{-0.044}$	38	14	$0.368^{+0.081}_{-0.074}$
875–1000	36	1	$0.028^{+0.017}_{-0.028}$	61	15	$0.246^{+0.059}_{-0.051}$	36	14	$0.389^{+0.083}_{-0.077}$

Notes. The first column indicates the upper boundary of each 75 pkpc concentric radial bin up to 375 pkpc, after which we assumed 125 pkpc concentric radial bin. The subsequent columns report the total number of galaxies surveyed in that annulus, the number of successful pairs detections, and the resulting covering fraction.

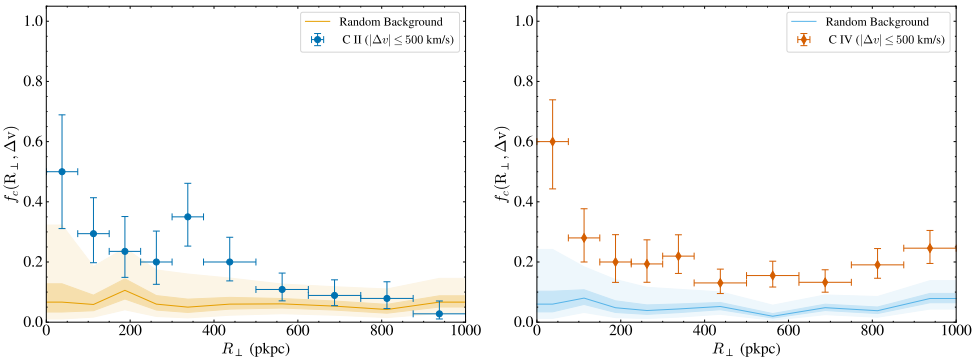

Fig. 3. Differential covering fraction of C II (left panel) and C IV (right panel) absorbers around the surveyed galaxies. The points represent the measured signal in concentric annuli. The vertical error bars denote the Wilson-score confidence interval of 1σ, while the horizontal error bars indicate the width of each radial bin. The solid line denotes the expected random background, and the light and dark shaded regions indicate the 1σ and 3σ confidence intervals, respectively.

described above. In Fig. 4 we show the cumulative covering fraction, assuming $\Delta v_{\mathrm{max}} = 500\,\mathrm{km\,s^{-1}}$, and computing the uncertainties as Wilson-score confidence interval of 1σ. The probability of finding a carbon absorber around an [O III] emitter is higher than 20% within 600 pkpc and then drops below 20% at distances up to maximum probe separations of ∼1 pMpc.

3.2. Carbon absorber-galaxy cross-correlation function

To capture the radial extent of the spatial clustering of the absorber-galaxy population, we evaluated the galaxy-absorber cross-correlation function (CCF). It quantifies the excess probability, relative to a random spatial distribution, of finding a C II or

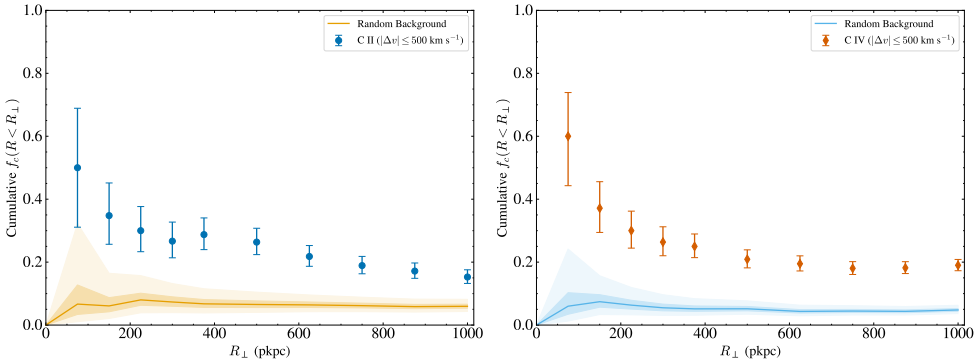

Fig. 4. Cumulative covering fraction of C II (left panel) and C IV (right panel) absorbers as a function of the impact parameter. The points represent the measured signal within a given radius. The solid line denotes the expected random background, where the light and dark shaded regions indicate the its 1σ and 3σ confidence intervals, respectively.

C IV absorber at a given comoving separation from a galaxy. We estimated the 3D CCF, denoted as $\xi(\Delta r)$, as a function of the 3D comoving distance between a galaxy and an absorber calculated as (e.g., D'Odorico et al. 2006)

$$\Delta \mathrm{r} = \sqrt{r_{g,\parallel}^2 + r_{a,\parallel}^2 - 2 r_{g,\parallel} r_{a,\parallel} \cos(\Delta\theta)}, \quad (7)$$

where $\mathrm{r}_{g,\parallel}$ and $\mathrm{r}_{a,\parallel}$ are the line-of-sight comoving distances to the galaxy and the absorber, derived from their respective redshifts assuming pure Hubble flow, and $\Delta\theta$ is their angular separation on the sky. We also note that because our distances are computed in redshift space, the physical clustering signal might be affected by redshift-space distortions. The proper motions of the galaxies, combined with the peculiar velocities of the gas relative to the host halos, induce an elongation along the line of sight. Thus, to compute the correlation function, we adopted the Peebles-Hauser estimator (Peebles & Hauser 1974; Vargas-Magaña et al. 2013),

$$\xi(\Delta r) = \frac{DD(\Delta r)}{DR(\Delta r)} \left(\frac{N_{DR}}{N_{DD}}\right) - 1, \quad (8)$$

where $DD(\Delta r)$ represents the number of observed galaxy-absorber pairs within a given comoving distance interval Δr, while $DR(\Delta r)$ is the expected number of random pairs in the same interval. The normalization factors N_{DD} and N_{DR} account for the total number of real and random pairs in the entire survey volume, respectively. We proceeded using the same conceptual shuffling technique as for the covering fraction for $DR(\Delta r)$ (see Sect. 3.1) by constructing a random catalog that accurately reproduced the survey geometry and selection function. Specifically, to compute the $DR(\Delta r)$ pairs, we cross-matched the angular coordinates of the galaxies observed in a given quasar field with the redshifts of the absorption systems detected along the sightlines of all the other EIGER fields. Finally, we computed the statistical uncertainties on the CCF considering the Poisson statistics as

$$\delta\xi(\Delta r) = \frac{1 + \xi(\Delta r)}{\sqrt{DD(\Delta r)}}. \quad (9)$$

We assumed comoving distance bins of 1.25 cMpc for the C II and C IV absorbers. These intervals were chosen to correspond to ~180 pkpc in proper distance, assuming a mean redshift of $z \sim 6$, compatible with the CGM scale. We report the values of the CCF computed for both ions in Table 3, and we show the corresponding results in Fig. 5.

To quantitatively describe this clustering profile and extract the characteristic correlation length, we modeled the measured $\xi(\Delta \mathrm{r})$ as a power law $\xi(\Delta \mathrm{r}) = (\Delta \mathrm{r}/\mathrm{r}_0)^{-\gamma}$, where r_0 is the correlation length, and γ is the power index. These two parameters are degenerate, and we therefore assumed typical values for γ adopted in the literature, $\gamma = 1.5$ and $\gamma = 1.8$ (Hennawi et al. 2006; Bielby et al. 2011; Trainor & Steidel 2012; Diener et al. 2017; García-Vergara et al. 2017, 2019; Galbiati et al. 2023). Thus, we obtained for the C II CCF a correlation length equal to $\mathrm{r}_0 = 3.60 \pm 0.73$ cMpc/h and for C IV we obtained $\mathrm{r}_0 = 4.09 \pm 0.74$ cMpc/h, assuming $\gamma = 1.8$. As discussed in previous studies (e.g., Trainor & Steidel 2012; Galbiati et al. 2023), the correlation length increases with decreasing slope of the power law. For $\gamma = 1.5$, the correlation lengths become $\mathrm{r}_0 = 4.52 \pm 0.87$ cMpc/h and $\mathrm{r}_0 = 5.60 \pm 0.75$ cMpc/h for C II and C IV, respectively. The correlation lengths of C II and C IV are consistent within 1σ, which implies that the two ionization phases share a similar large-scale clustering amplitude around high-redshift [O III] emitters.

3.3. Galaxy-galaxy autocorrelation function

To quantify the spatial clustering of the population of [O III] emitters we considered, we computed the 3D galaxy-galaxy autocorrelation function (ACF), $\xi_{GG}(\Delta r)$. The ACF was computed by comparing the observed pair counts with those expected from a random distribution, subject to the exact same observational constraints. The random pairs were obtained by generating a synthetic random catalog of 500 galaxies whose angular coordinates were uniformly sampled within the same field of view of the observations. It is also important to note that we generated synthetic random galaxies without masking bright foreground objects since they only occupy small regions compared to the overall field of view. This does not affect our result much because of the high number of galaxies generated. Furthermore, the redshifts of the random galaxies were extracted from a Gaussian kernel density estimator (KDE) fitted to the redshift distribution of the full observed galaxy sample. We then calculated the comoving distance for all data-data (DD) and random-random (RR) pairs within each field with the same method as for the carbon absorber-galaxy CCF (see Section 3.2). We assumed a comoving distance bin of 1.0 cMpc. We show our 3D galaxy-galaxy ACF in Fig. 5.

A clear and strong clustering signal was detected at a comoving distance $R < 2.5$ cMpc, reaching a significance of $\sim 13\sigma$, as expected for galaxy populations that are not randomly distributed in the Universe. Moreover, a weaker but highly statistically significant ($\gtrsim 10\sigma$) extended signal was observed up to 7.5 cMpc, probably due to the peculiar galaxy velocities and large-scale structures. Furthermore, following the method applied to the CCF, we modeled the measured galaxy-galaxy ACF as a power law, finding the characteristic correlation lengths of $r_0^{GG} = 10.63 \pm 0.56$ cMpc/h and $r_0^{GG} = 7.84 \pm 0.84$ cMpc/h assuming $\gamma = 1.5$ and $\gamma = 1.8$, respectively.

Table 3. C II and C IV absorber galaxy cross-correlation function values.

Δr cMpc/h	C II DD(Δr)	C II DR(Δr)	C II $\xi(\Delta r)$	C IV DD(Δr)	C IV DR(Δr)	C IV $\xi(\Delta r)$
0–1.25	3	1	12.20 ± 7.62	7	2	16.24 ± 6.52
1.25–2.5	14	7	7.80 ± 2.35	20	11	7.96 ± 2.00
2.5–3.75	6	5	4.28 ± 2.16	10	17	1.90 ± 0.92
3.75–5.0	13	28	1.04 ± 0.57	17	23	2.64 ± 0.8
5.0–6.25	10	35	0.26 ± 0.40	16	33	1.39 ± 0.60
6.25–7.5	15	34	0.94 ± 0.50	21	50	1.07 ± 0.45

Notes. The first column indicates the comoving distance bin, and the second and third columns represent the number of galaxy-absorber real and random pairs found in that specific bin. Finally, the last column denotes the cross-correlation function.

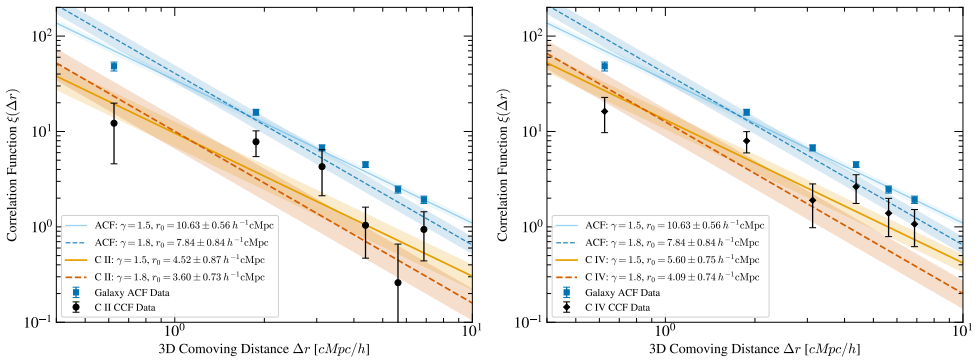

Fig. 5. 3D C II (left panel) and C IV (right panel) absorber-[O III] emitting galaxy CCF as a function of the comoving distance at $z \sim 6$. The black points represent the measured signal, with vertical error bars indicating the 1σ Poisson error. The solid orange and dotted red lines represent the best-fit power laws with index $\gamma = 1.5$ and 1.8, respectively. The shaded orange and red regions denote the associated 1σ confidence intervals. The blue squares denote the ACF of the [O III] emitters. The solid and dotted blue lines represent the best-fit power laws with index $\gamma = 1.5$ and 1.8, respectively.

For $\gamma = 1.5$, the correlation lengths obtained for ACF are higher by a factor of 2.4 and 1.9 than those obtained for C II and C IV galaxy-absorber CCFs, respectively. The two functions exhibit neither similar shapes nor the same amplitude in the EIGER fields. Based on these findings, the data therefore do not support the scenario in which [O III] emitters, C II and C IV absorbers exclusively trace the exact same regions of the Universe. This might also suggest that a fraction of the low- and high-ionization metals is not exclusively confined to the halos of star-forming galaxies, but is instead distributed within the intergalactic medium or associated with a population of undetected faint dwarf galaxies.

However, previous studies have been conducted on the galaxy-galaxy autocorrelation function. Using a partially overlapping dataset of galaxies in a redshift range of $5.95 \leq z \leq 6.55$ and in five of the six EIGER fields, Eilers et al. (2023) reported a correlation length in the real space of $r_0^{GG} = 4.1 \pm 0.3$ cMpc/h assuming $\gamma = 1.8$. Their analysis employed the volume-averaged projected correlation function, integrating pairs with $\Delta v < 1000\,\mathrm{km\,s^{-1}}$, to suppress the effects of galaxies peculiar velocities and redshift uncertainties. While projected statistics are optimal for recovering the underlying real-space clustering of galaxies, our primary objective was to perform a strict self-consistent comparison between the galaxy-galaxy ACF and absorber-galaxy CCF clustering. By computing the ACF and the CCF in 3D redshift space using the exact same metric and method, we ensured that both measurements were subject to the same line-of-sight distortions, making their relative comparison reliable.

3.4. Equivalent width profile

To explore how the absorption strength is shaped by the proximity to star-forming galaxies, we investigated the radial profile of the absorber equivalent widths. Previous studies found indications of an anticorrelation between the rest-frame equivalent width (REW) of C IV and the impact parameter of the associated galaxy. Most of these works focused on lower-redshift galaxy samples: at $z \leq 1$ (Chen et al. 2001; Bordoloi et al. 2014; Burchett et al. 2016), $z \leq 1.5$–2 (Dutta et al. 2020), and at $z \sim 3$–4 (Galbiati et al. 2023). We extend the study of the radial profile of the C IV absorption strength to $z \sim 6$, and we compare it to that of the C II absorbers for the first time, following the procedure described in Dutta et al. (2020). The REW is expected to decrease with increasing $R_\perp$ following a log-linear relation that reproduces a sudden drop in absorption strength, scaled by a factor related to the virial galaxy radius,

$$\log(W_r/\text{Å}) = a + b \cdot (R_\perp/\text{kpc}). \tag{10}$$

In the computation, we used REW measurements and 3σ upper limits determined as

$$EW_{\text{min,obs}} \approx \frac{3 \times \lambda_{\text{ion,obs}}}{R \times (S/N)_{\text{pix}} \times \sqrt{n_{\text{samp}}}}, \tag{11}$$

where EW_{min} is the minimum observable equivalent width (in Å) that can be reliably detected above the noise level, $\lambda_{\text{obs,ion}}$ is the

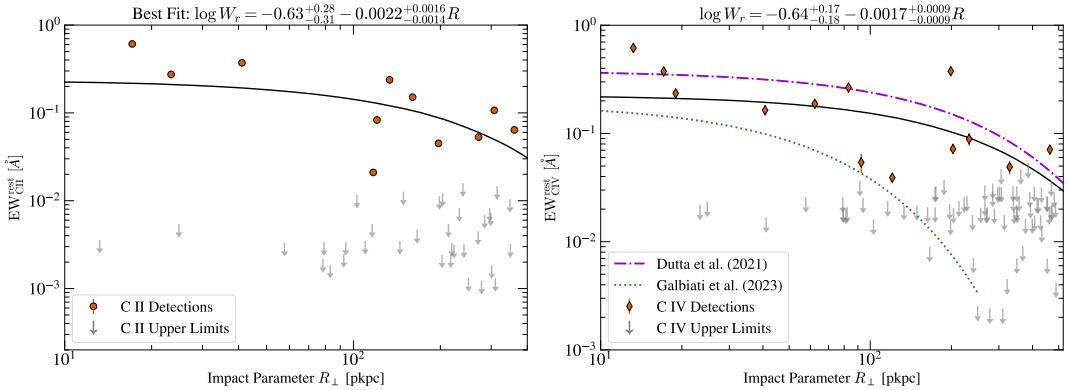

Fig. 6. EW profile as a function of transverse separation from the associated galaxy, $R_\perp$, for the C II (left panel) and the C IV (right panel) absorption systems. The circles and diamonds indicate C II and C IV detections, respectively. The 1σ uncertainties on the rest-frame EW are typically smaller than the symbol size. The gray arrows indicate 3σ upper limits in the EW of the two carbon ions for all the galaxies that are not associated with any absorber. The best result of a log-linear fit is drawn as a solid black line, and the 1σ uncertainties are marked by shaded regions. In the right panel, we compare the results obtained for the C IV absorbers with the best-fit relation from Galbiati et al. (2023, green dotted line) at z = 3–4 and Dutta et al. (2021, purple dash-dotted line) at $z < 2$.

central wavelength of the absorption feature, R is the resolving power of the spectrograph, $(\mathrm{S/N})_{\mathrm{pix}}$ is the median signal-to-noise ratio per pixel in the continuum of the spectrum near to the absorption feature, and finally, n_{samp} is the number of pixels that sample the spectral resolution element. Upper limits were determined at the redshift of all galaxies that did not show an associated C II or C IV absorber within 500 pkpc from the line of sight (see Table A.1) only for the quasars for which the spectra were available. To compute the $(\mathrm{S/N})_{\mathrm{pix}}$, we considered a wavelength interval of ± 1000 km s^{-1}, centered on $\lambda_{\mathrm{ion,obs}}$, avoiding other absorption or emission features present in the spectrum. The resolving power for J0148, J0100, and J1030 was provided by D'Odorico et al. (2023), while we derived the value from our analysis described in Appendix B for J159. The resolution for J1148 and J1120 was provided by Becker et al. (2006) and Bosman et al. (2017), respectively. Finally, n_{samp} was computed as $n_{\mathrm{samp}} = c/(10 \times R)$.

We fit the equivalent width profile including detections and upper limits with the function in Equation (10) by applying a Bayesian method based on the product of two likelihood functions, one for measurements and the other for upper limits, as described in Dutta et al. (2020, 2021) (for more details, see also Chen et al. 2010; Rubin et al. 2018; Galbiati et al. 2023). We note that our sample shows a disparity in terms of number of detections and upper limits, especially at larger impact parameters. To take this disparity into account, we split the likelihood for the upper limits into two parts raised to two different factors, α_1 and α_2, respectively, considered as free parameters in the fit. The first likelihood refers to the upper limits within $R_\perp < 100$ pkpc and the second to those at $R_\perp > 100$ pkpc. This choice was motivated by the fact that we observed only 3 detections with 10 upper limits within 100 pkpc, and 8 detections with 27 upper limits for $R_\perp > 100$ pkpc for C II, while for C IV we have 7 detections and 10 upper limits within 100 pkpc and 6 detections and 68 upper limits at $R_\perp > 100$ pkpc. We derived posterior probability distributions and the Bayesian evidence with the nested-sampling Monte Carlo algorithm MLFriends (Buchner et al. 2014; Buchner 2019) using the UltraNest[1] package (Buchner 2021). The results are shown in Fig. 6 as solid lines, and the shaded blue region marks the 1σ confidence level.

[1] https://johannesbuchner.github.io/UltraNest/

4. Discussion

We have extended the comparison between a statistical sample of C II and C IV absorption systems and the galaxies distributed over six fields centered on $z \sim 6$ quasars to $z > 5$ for the first time. Many previous studies investigated the same topic at lower redshift (Adelberger et al. 2005; Dutta et al. 2021; Muzahid et al. 2021; Schroetter et al. 2021; Banerjee et al. 2023; Galbiati et al. 2023, 2024), in most cases identifying galaxies as Lyα emitters. The general conclusion of most of these works is that the metal absorption around galaxies is significantly higher (extending to separations of ~100−200 pkpc) and that this enhancement is more significant for galaxies in groups than for isolated galaxies. Although we lack the statistics with our sample to distinguish between the signal from isolated and group galaxies, we note that C IV absorption systems are preferentially associated with large groups of galaxies.

4.1. Redshift evolution of the C IV and galaxy relation

We investigated the signatures of the redshift evolution for C IV absorption systems using the *Quasar Sightline and Galaxy Evolution* (QSAGE) sample from Dutta et al. (2021) at $z < 2$ and the *MUSE Analysis of Gas around Galaxies* (MAGG) sample from Galbiati et al. (2023) at $z \sim$ 3–4, for which we were able to carry out the analysis in exactly the same way as for our sample. However, in QSAGE, the galaxies are identified from their continuum emission and in some cases from the [O II] emission, and they have a median stellar mass of $\mathrm{M}_\star \approx 2 \times 10^9\,\mathrm{M}_\odot$ and a median SFR of $1.5\,\mathrm{M}_\odot\,\mathrm{yr}^{-1}$ (Dutta et al. 2021). In MAGG, instead, galaxies are Lyα emitters. These ranges of galaxy properties are comparable with the [O III] emitters found in the EIGER fields. In order to carry out a consistent analysis, we considered absorption systems in the three samples with a C IV REW $\geq$ 0.05 Å. In Fig. 6 we compare the REW radial profile of C IV absorbers in our sample with those by Dutta et al. (2021) and Galbiati et al. (2023). The shape of the profile by Dutta et al. (2021) is similar to our shape, but with a larger normalization, while the normalization of the profile by Galbiati et al. (2023) agrees with our result, but the shape differs, showing a turnaround on smaller scales. This might be due to the smaller spatial extent of VLT/Multi Unit Spectroscopic Explorer (MUSE, Bacon et al. 2010) field of view in MAGG with respect

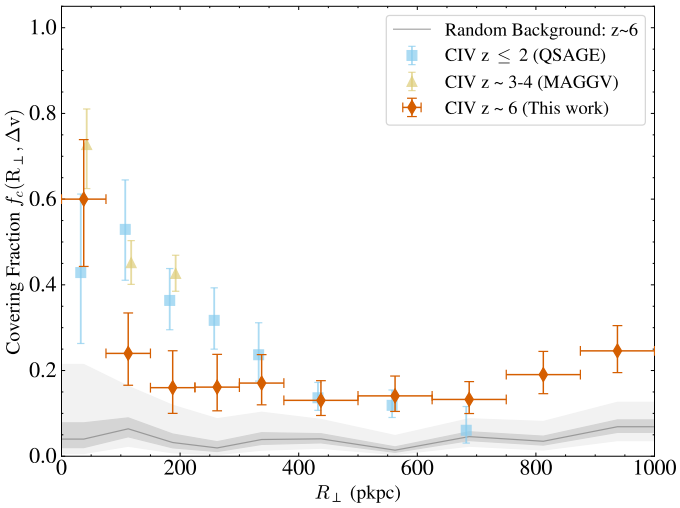

Fig. 7. C IV covering fraction comparison between this work (orange diamonds) and lower-redshift samples: the QSAGE survey at $z \leq 2$ (light blue squares, Dutta et al. 2021), and the MAGG survey at $z \sim 3$–4 (green triangles, Galbiati et al. 2023). All the errors represent 1σ Wilson-score confidence intervals.

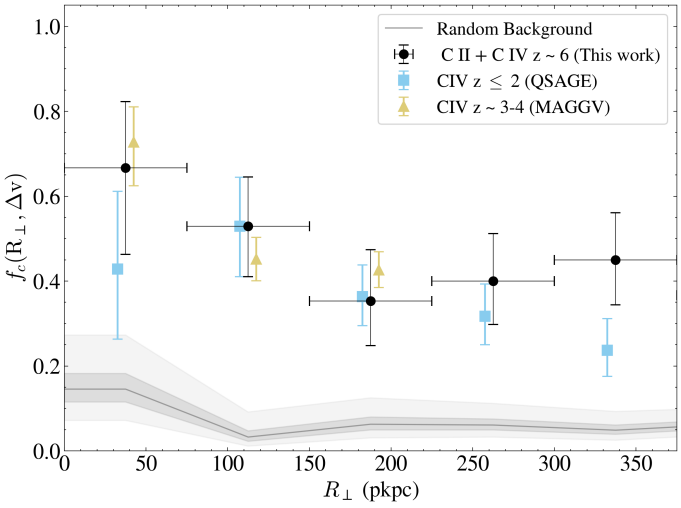

Fig. 8. Same as Fig. 7 but comparing the low-redshift C IV covering fractions with the C II + C IV covering fraction from this work (black circles). All the errors represent 1σ Wilson-score confidence intervals.

to those of QSAGE and EIGER, however. Given the small size of our sample and the different tracers used to identify galaxies in the three samples, it is challenging and ambiguous to perform a direct comparison between these results and to draw any conclusion about a possible redshift evolution (Galbiati et al. 2023).

Figure 7 shows the comparison of the C IV covering fraction for the three samples. In the first impact parameter bin ($R_\perp < 75$ pkpc), the C IV covering fraction at $z \sim 6$ is consistent within the errors with the values observed at lower redshift. This means that the highly ionized metal-enriched gas traced by C IV is already present in the vicinity of galaxies at the end of reionization. However, at larger impact parameters, the $z \sim 6$ data show an evident drop compared with the lower-redshift samples. This strong difference at intermediate impact parameters ($75 \leq R_\perp \leq 400$ pkpc) might suggest a cosmic evolution in the extension of the C IV enriched sphere around galaxies. However, the interpretation of this result needs to take the rapid decline in the number density of C IV absorption systems into account that is observed at $z > 5$ (e.g., Ryan-Weber et al. 2009; Simcoe et al. 2011; D'Odorico et al. 2013; Codoreanu et al. 2018; D'Odorico et al. 2022; Davies et al. 2023b), accompanied by an increase in the number density of low-ionization lines (O I and C II, Becker et al. 2019; Sebastian et al. 2024). This has been explained by the change in the ionization state of the IGM and CGM gas due to the last phases of the reionization process. The observed drop in the $z \sim 6$ covering fraction might be an effect of the change in the ionization state of the CGM at these redshifts and not a difference in the distribution of the metal-enriched gas. We tested this hypothesis by combining the covering fraction due to C IV and C II, avoiding double counting when both transitions were observed at the same redshift, and restricting the redshift coverage to that of C II (see Table 2). The resulting covering fraction, shown in Fig. 8, now agrees with those at lower redshift out to ≃400 pkpc. Our interpretation is that low-ionization gas traced by C II significantly contributes to the CGM of $z \sim 6$ galaxies out to larger separations than to what happens at z after the end of the reionization process. A decisive test would be the implementation of the C II + C IV covering fraction at lower redshift as well; we will explore this topic in a future work.

It is important to highlight that our measured carbon-covering fractions is related to the selection function of our galaxy sample, dominated by galaxies identified via strong [O III] emission. This technique preferentially selects young actively star-forming and relatively metal-enriched systems. Since [O III] emitters undergo starburst-driven feedback, they are expected to launch powerful galactic winds. These outflows actively transport metal-enriched material from the interstellar medium into the halo, likely boosting the observed covering fractions of C II and C IV at intermediate and large impact parameters compared to a quiescent or more weakly star-forming galaxy population.

4.2. Carbon mass budget at z ~ 6

Finally, we derived a conservative lower limit for the total carbon mass associated with [O III]-emitting galaxies. Following the approach adopted by Bordoloi et al. (2014) and Higginson et al. (2026), the mass of specific carbon ions contained in an annulus within an inner radius $R_{\rm in}$ and outer radius $R_{\rm out}$ is

$$M_{\rm ion} = \frac{1}{f_{\rm ion}} f_c \pi (R_{\rm out}^2 - R_{\rm in}^2) \langle N_{\rm ion} \rangle \; m_{\rm C}, \tag{12}$$

where f_c is the covering fraction, $\langle N_{\rm ion} \rangle$ is the mean column density in the annulus, and $m_{\rm C} = 12 m_p$ is the mass of carbon atoms, while m_p is the proton mass.

To ensure that our estimate remained a robust lower limit, we set the ionization fraction to $f_{\rm ion} = 0.5$ for both ions. Setting $f_{\rm ion} = 0.5$ implies that all carbon resides exclusively in the C II and C IV states, completely neglecting other ionization stages, most notably C III λ977 Å which is expected to be an important fraction in diffuse CGM (Tumlinson et al. 2017). It is particularly challenging to account for C III because its main resonant transition falls within the Lyα forest, which at these redshifts becomes completely opaque due to the Gunn-Peterson effect (Gunn & Peterson 1965; Fan et al. 2006). For these reasons, the resulting mass must be strictly interpreted as the mass of the observed carbon and not a complete mass budget. With these caveats in mind, we computed masses of each ion in two radial bins: 0–100 pkpc and 100–300 pkpc, respectively. The total mass was obtained by summing the two contributions in the two annuli

considered. We found that the total C II + C IV mass obtained as a lower limit at $z \sim 6$ is $\geq 2.8 \times 10^6\,M_\odot$ within $R_{\rm max} = 300$ pkpc. This value is very similar to the total mass in oxygen obtained by Higginson et al. (2026) of $M_O \geq 2 \times 10^6\,M_\odot$ in the same $R_{\rm max}$, considering that all oxygen is in the form of neutral oxygen, justifying this assumption due to the tight charge-exchange coupling with HI and the negligible dust depletion of oxygen (Bordoloi et al. 2017; Higginson et al. 2026).

5. Conclusions

We investigated the connection between cool and ionized gas phases, traced by C II and C IV absorption-line systems in quasar spectra, and a population of [O III] emitting galaxies, at $5.30 < z < 6.97$, identified in the EIGER survey, during the epoch of reionization. We traced these multiphase environments by assembling a sample of 16 C II and 14 C IV absorbers in the redshift range $5.33 < z < 6.52$. Within a velocity separation of $|\Delta v| \leq 500\,{\rm km\,s^{-1}}$ and an impact parameter of $R_\perp \leq 1000$ pkpc, we found 44 [O III] emitters around C II absorbers and 92 [O III] emitters from C IV absorbers. Leveraging these two samples, we were able to probe the multiphase nature of the CGM deep into the Epoch of Reionization for the first time by comparing two distinct ionization states of carbon. We detected an excess in the C II and C IV absorbers around galaxies compared to random expectations, confirming that low- and high-ionization carbon are both physically associated with galaxies at $z \sim 6$. The covering fraction of both ions decreases with increasing impact parameter, although C IV remains detectable over larger projected distances than C II, suggesting that the warm ionized phase is more spatially extended than the cooler gas.

The galaxy-absorber cross-correlation analysis revealed strong clustering for both ions. We measured correlation lengths of $r_0 = 3.60 \pm 0.73\,{\rm cMpc\,h^{-1}}$ for C II and $r_0 = 4.09 \pm 0.74\,{\rm cMpc\,h^{-1}}$ for C IV assuming $\gamma = 1.8$, and $r_0 = 4.52 \pm 0.87\,{\rm cMpc\,h^{-1}}$ for C II and $r_0 = 5.60 \pm 0.75\,{\rm cMpc\,h^{-1}}$ for C IV assuming $\gamma = 1.5$. However, the galaxy-absorber correlation remained significantly weaker than the [O III] emitters autocorrelation function, which has a correlation length of $r_0^{GG} = 7.84 \pm 0.84\,{\rm cMpc\,h^{-1}}$ assuming $\gamma = 1.8$, and $r_0^{GG} = 10.63 \pm 0.56\,{\rm cMpc\,h^{-1}}$ assuming $\gamma = 1.5$. This suggests that a fraction of low- and high-ionization carbon is not exclusively confined to the halos of massive galaxies, but is likely distributed throughout the surrounding large-scale environment or associated with galaxies fainter than the detection limit of the EIGER survey (40% complete at $L_{5008} = 10^{42}\,{\rm erg\,s^{-1}}$).

The equivalent width profiles of both ions decline with increasing impact parameter. C IV appears to be consistent with previous measurements at lower redshift, such as QSAGE at $z \leq 2$ and MAGG at $z \sim 3$–4. In particular, the C IV profile agrees with measurements from the MAGG survey until 100 pkpc, suggesting that the radial distribution of highly ionized carbon around galaxies may already be largely established by the end of the EoR.

In addition, we derived a conservative lower limit on the observed carbon mass associated with galaxies of $M_{\rm C\,II+C\,IV} \simeq 2.8 \times 10^6\,M_\odot$ within 300 pkpc. Since our estimate neglects unobserved ionization states, particularly C III, it should be interpreted as a lower limit to the observed carbon reservoir and not as the total carbon budget of the CGM.

Finally, by comparing our measurements with lower-redshift surveys, we found that the C IV covering fraction at small impact parameters is already comparable to that observed at later cosmic times, while it declines more rapidly at intermediate distances. This behavior is consistent with the observed evolution of the cosmic abundance of carbon ions and supports a scenario in which a larger fraction of circumgalactic carbon resides in lower ionization states during the epoch of reionization.

Overall, our results provide one of the first statistical characterizations of the multiphase CGM around star-forming galaxies during the epoch of reionization using two ionization states of the same element. They indicate that chemically enriched gas was already widespread around galaxies at $z \sim 6$ and simultaneously suggests that the ionization structure and spatial distribution of circumgalactic metals were still evolving. In a future paper (Galbiati et al. in prep.), we will investigate the connection between absorbers and galaxies identified through Lyα emission over more than 30 fields of quasars at $z \sim 6$. It would also be desirable to increase the number of quasar fields studied with JWST with the same approach as adopted in the EIGER survey. All these studies would enable a more complete picture of the multiphase CGM and its role in the early assembly of galaxies.

Acknowledgements. We thank the referee for the careful reading of this paper and the suggestions which improved the manuscript. CP, VD, KK, LPe, LPa, and RR acknowledge support from the ERC synergy grant 101166930 – RECAP. FS acknowledges financial support from the Bando Finanziamento ASI CI-UCO-DSR-2022-43 CUP:C93C25004260005 project "IBISCO: feedback and obscuration in local AGN", the Ricerca Fondamentale INAF 2023 Data Analysis grant 1.05.23.03.04 "ARCHIE ARchive Cosmic HI & ISM Evolution", Ricerca Fondamentale INAF 2024 under project 1.05.24.07.01 MINI-GRANTS RSN1 "ECHOS". CM acknowledges support from Fondecyt Iniciacion grant 11240336 and the ANID BASAL project FB210003. This work is based on observations collected at the European Southern Observatory under ESO programmes 098.B-0537(A) and 0114.B-0278(A). This work is based on observations made with the NASA/ESA/CSA James Webb Space Telescope. The data were obtained from the Mikulski Archive for Space Telescopes at the Space Telescope Science Institute, which is operated by the Association of Universities for Research in Astronomy, Inc., under NASA contract NAS 5-03127 for JWST. These observations are associated with program #1243. This research made use of `Astropy` (Astropy Collaboration 2013, 2018, 2022), `scipy` (Virtanen et al. 2020), `numpy` (Harris et al. 2020), `lmfit` (Newville et al. 2025), `matplotlib` (Hunter 2007), and `pandas` (McKinney 2010).

References

Adelberger, K. L., Shapley, A. E., Steidel, C. C., et al. 2005, ApJ, 629, 636
Astropy Collaboration (Robitaille, T. P., et al.) 2013, A&A, 558, A33
Astropy Collaboration (Price-Whelan, A. M., et al.) 2018, AJ, 156, 123
Astropy Collaboration (Price-Whelan, A. M., et al.) 2022, ApJ, 935, 167
Bacon, R., Accardo, M., Adjali, L., et al. 2010, SPIE Conf. Ser., 7735, 773508
Bañados, E., Venemans, B. P., Decarli, R., et al. 2016, ApJS, 227, 11
Bañados, E., Mazzucchelli, C., Momjian, E., et al. 2021, ApJ, 909, 80
Banerjee, E., Muzahid, S., Schaye, J., Johnson, S. D., & Cantalupo, S. 2023, MNRAS, 524, 5148
Banerjee, E., Muzahid, S., Schaye, J., et al. 2025, ApJ, 980, 171
Banerjee, E., Muzahid, S., Schaye, J., Johnson, S. D., & Cantalupo, S. 2026, MNRAS, submitted [arXiv:2601.07916]
Becker, G. D., Sargent, W. L. W., Rauch, M., & Simcoe, R. A. 2006, ApJ, 640, 69
Becker, G. D., Pettini, M., Rafelski, M., et al. 2019, ApJ, 883, 163
Bielby, R. M., Shanks, T., Weilbacher, P. M., et al. 2011, MNRAS, 414, 2
Bischetti, M., Fiore, F., Feruglio, C., et al. 2023, ApJ, 952, 44
Bordoloi, R., Tumlinson, J., Werk, J. K., et al. 2014, ApJ, 796, 136
Bordoloi, R., Fox, A. J., Lockman, F. J., et al. 2017, ApJ, 834, 191
Bordoloi, R., Simcoe, R. A., Matthee, J., et al. 2024, ApJ, 963, 28
Bosman, S. E. I., Becker, G. D., Haehnelt, M. G., et al. 2017, MNRAS, 470, 1919
Buchner, J. 2019, PASP, 131, 108005
Buchner, J. 2021, J. Open Source Softw., 6, 3001
Buchner, J., Georgakakis, A., Nandra, K., et al. 2014, A&A, 564, A125
Burchett, J. N., Tripp, T. M., Bordoloi, R., et al. 2016, ApJ, 832, 124
Chen, H.-W., Lanzetta, K. M., & Webb, J. K. 2001, ApJ, 556, 158
Chen, H.-W., Helsby, J. E., Gauthier, J.-R., et al. 2010, ApJ, 714, 1521
Chen, S.-F. S., Simcoe, R. A., Torrey, P., et al. 2017, ApJ, 850, 188

Christensen, L., Jakobsen, P., Willott, C., et al. 2023, A&A, 680, A82
Clough, S., Shephard, M., Mlawer, E., et al. 2005, J. Quant. Spectrosc. Radiat. Transf., 91, 233
Coatman, L., Hewett, P. C., Banerji, M., et al. 2017, MNRAS, 465, 2120
Codoreanu, A., Ryan-Weber, E. V., Garcia, L. A., et al. 2018, MNRAS, 481, 4940
Cupani, G., D'Odorico, V., Cristiani, S., et al. 2020, Proc. SPIE, 11452, 114521U
Cupani, G., D'Odorico, V., Cristiani, S., et al. 2022, ASP Conf. Ser., 532, 207
Davies, R. L., Ryan-Weber, E., D'Odorico, V., et al. 2023a, MNRAS, 521, 289
Davies, R. L., Ryan-Weber, E., D'Odorico, V., et al. 2023b, MNRAS, 521, 314
De Rosa, G., Decarli, R., Walter, F., et al. 2011, ApJ, 739, 56
Dean, N., & Pagano, M. 2015, J. Surv. Stat. Methodol., 3, 484
Decarli, R., Falomo, R., Treves, A., et al. 2010, MNRAS, 402, 2453
Decarli, R., Walter, F., Venemans, B. P., et al. 2018, ApJ, 854, 97
Dekel, A., Sari, R., & Ceverino, D. 2009, ApJ, 703, 785
Díaz, C. G., Ryan-Weber, E. V., Karman, W., et al. 2021, MNRAS, 502, 2645
Diener, C., Wisotzki, L., Schmidt, K. B., et al. 2017, MNRAS, 471, 3186
Dietrich, M., Hamann, F., Appenzeller, I., & Vestergaard, M. 2003, ApJ, 596, 817
D'Odorico, V., Viel, M., Saitta, F., et al. 2006, MNRAS, 372, 1333
D'Odorico, V., Cupani, G., Cristiani, S., et al. 2013, MNRAS, 435, 1198
D'Odorico, V., Finlator, K., Cristiani, S., et al. 2022, MNRAS, 512, 2389
D'Odorico, V., Bañados, E., Becker, G. D., et al. 2023, MNRAS, 523, 1399
Dutta, R., Fumagalli, M., Fossati, M., et al. 2020, MNRAS, 499, 5022
Dutta, R., Fumagalli, M., Fossati, M., et al. 2021, MNRAS, 508, 4573
Eilers, A.-C., Simcoe, R. A., Yue, M., et al. 2023, ApJ, 950, 68
Fan, X., Strauss, M. A., Becker, R. H., et al. 2006, AJ, 132, 117
Farina, E. P., Arrigoni-Battaia, F., Costa, T., et al. 2019, ApJ, 887, 196
Farina, E. P., Schindler, J.-T., Walter, F., et al. 2022, ApJ, 941, 106
Faucher-Giguère, C.-A., & Oh, S. P. 2023, ARA&A, 61, 131
Ford, A. B., Oppenheimer, B. D., Davé, R., et al. 2013, MNRAS, 432, 89
Fumagalli, M., O'Meara, J. M., Prochaska, J. X., Rafelski, M., & Kanekar, N. 2015, MNRAS, 446, 3178
Galbiati, M., Fumagalli, M., Fossati, M., et al. 2023, MNRAS, 524, 3474
Galbiati, M., Dutta, R., Fumagalli, M., Fossati, M., & Cantalupo, S. 2024, A&A, 690, A7
García-Vergara, C., Hennawi, J. F., Felipe Barrientos, L., & Rix, H.-W. 2017, ApJ, 848, 7
García-Vergara, C., Hennawi, J. F., Barrientos, L. F., & Battaia, F. A. 2019, ApJ, 886, 79
Gullikson, K., Dodson-Robinson, S., & Kraus, A. 2014, AJ, 148, 53
Gunn, J. E., & Peterson, B. A. 1965, ApJ, 142, 1633
Harris, C. R., Millman, K. J., van der Walt, S. J., et al. 2020, Nature, 585, 357
Hennawi, J. F., Strauss, M. A., Oguri, M., et al. 2006, AJ, 131, 1
Higginson, J., Bordoloi, R., Simcoe, R. A., et al. 2026, ApJ, 999, 49
Ho, S. H., Martin, C. L., & Schaye, J. 2021, ApJ, 923, 137
Horne, K. 1986, PASP, 98, 609
Hunter, J. D. 2007, Comput. Sci. Eng., 9, 90
Kashino, D., Lilly, S. J., Matthee, J., et al. 2023, ApJ, 950, 66
Kashino, D., Lilly, S. J., Matthee, J., et al. 2026, ApJ, 997, 280
Maiolino, R., Cox, P., Caselli, P., et al. 2005, A&A, 440, L51
Matthee, J., Mackenzie, R., Simcoe, R. A., et al. 2023, ApJ, 950, 67
Mazzucchelli, C., Bañados, E., Venemans, B. P., et al. 2017, ApJ, 849, 91
Mazzucchelli, C., Bischetti, M., DOdorico, V., et al. 2023, A&A, 676, A71
McKinney, W. 2010, in Proceedings of the 9th Python in Science Conference, eds. S. van der Walt, & J. Millman, 56
McLean, I. S., Steidel, C. C., Epps, H., et al. 2010, Proc. SPIE, 7735, 77351E
Muzahid, S., Schaye, J., Cantalupo, S., et al. 2021, MNRAS, 508, 5612
Newville, M., Otten, R., Nelson, A., et al. 2025, https://doi.org/10.5281/zenodo.598352
Onoue, M., Bañados, E., Mazzucchelli, C., et al. 2020, ApJ, 898, 105
Oppenheimer, B. D., & Davé, R. 2008, MNRAS, 387, 577
Peebles, P. J. E., & Hauser, M. G. 1974, ApJS, 28, 19
Péroux, C., & Howk, J. C. 2020, ARA&A, 58, 363
Prochaska, J. X., Hennawi, J., Cooke, R., et al. 2019, Astrophysics Source Code Library [record ascl:1911.004]
Prochaska, J., Hennawi, J., Westfall, K., et al. 2020, J. Open Source Softw., 5, 2308
Qu, Z., Chen, H.-W., Rudie, G. C., et al. 2023, MNRAS, 524, 512
Rieke, M. J., Kelly, D. M., Misselt, K., et al. 2023, PASP, 135, 028001
Rousselot, P., Lidman, C., Cuby, J.-G., Moreels, G., & Monnet, G. 2000, A&A, 354, 1134
Rubin, K. H. R., Diamond-Stanic, A. M., Coil, A. L., Crighton, N. H. M., & Moustakas, J. 2018, ApJ, 853, 95
Rudie, G. C., Steidel, C. C., Trainor, R. F., et al. 2012, ApJ, 750, 67
Rudie, G. C., Steidel, C. C., Pettini, M., et al. 2019, ApJ, 885, 61
Ryan-Weber, E. V., Pettini, M., Madau, P., & Zych, B. J. 2009, MNRAS, 395, 1476
Schindler, J.-T., Farina, E. P., Bañados, E., et al. 2020, ApJ, 905, 51
Schroetter, I., Bouché, N. F., Zabl, J., et al. 2021, MNRAS, 506, 1355
Sebastian, A. M., Ryan-Weber, E., Davies, R. L., et al. 2024, MNRAS, 530, 1829
Shen, Y., Richards, G. T., Strauss, M. A., et al. 2011, ApJS, 194, 45
Shin, J., Nagao, T., Woo, J.-H., & Le, H. A. N. 2019, ApJ, 874, 22
Simcoe, R. A., Burgasser, A. J., Bernstein, R. A., et al. 2008, Proc. SPIE, 7014, 70140U
Simcoe, R. A., Cooksey, K. L., Matejek, M., et al. 2011, ApJ, 743, 21
Steidel, C. C., Erb, D. K., Shapley, A. E., et al. 2010, ApJ, 717, 289
Trainor, R. F., & Steidel, C. C. 2012, ApJ, 752, 39
Tumlinson, J., Peeples, M. S., & Werk, J. K. 2017, ARA&A, 55, 389
Turner, M. L., Schaye, J., Steidel, C. C., Rudie, G. C., & Strom, A. L. 2014, MNRAS, 445, 794
van Dokkum, P. G. 2001, PASP, 113, 1420
Vargas-Magaña, M., Bautista, J. E., Hamilton, J.-C., et al. 2013, A&A, 554, A131
Venemans, B. P., Walter, F., Neeleman, M., et al. 2020, ApJ, 904, 130
Vernet, J., Dekker, H., D'Odorico, S., et al. 2011, A&A, 536, A105
Vestergaard, M., & Osmer, P. S. 2009, ApJ, 699, 800
Vestergaard, M., & Peterson, B. M. 2006, ApJ, 641, 689
Vestergaard, M., & Wilkes, B. J. 2001, ApJS, 134, 1
Virtanen, P., Gommers, R., Oliphant, T. E., et al. 2020, Nat. Methods, 17, 261
Vogt, S. S., Allen, S. L., Bigelow, B. C., et al. 1994, Instrumentation in Astronomy VIII (SPIE), 2198, 362
Wang, F., Yang, J., Hennawi, J. F., et al. 2023, ApJ, 951, L4
Weng, S., Péroux, C., Ramesh, R., et al. 2024, MNRAS, 527, 3494
Wilson, E. B. 1927, J. Am. Stat. Assoc., 22, 209
Yang, J., Wang, F., Fan, X., et al. 2021, ApJ, 923, 262
Zou, S., Cai, Z., Wang, F., et al. 2024, ApJ, 963, L28

Appendix A: Carbon absorbers with associated [O III] emitters

Table A.1. C II and C IV absorption systems with $\log(N) + \sigma_{\log(N)} \geq 13.0$, and their associated galaxies in the EIGER survey fields identified within $R_\perp \leq 1000$ pkpc and $|\Delta v| < 500$ km s^{-1}.

Quasar Field	z_{abs}	$\log(N_{C\,II})$ cm^{-2}	$\log(N_{C\,IV})$ cm^{-2}	Gal ID	z_{gal}	$R_\perp$ pkpc	Δv km s^{-1}	Δr cMpc
J0148	5.48774	<12.09	13.17 ± 0.13	19570	5.490	92.6	104.4	1.27
		<12.09		19764	5.490	292.1	104.4	2.20
J1030	5.51737	-	13.74 ± 0.07	7771	5.519	40.7	-75.0	0.85
				7594	5.516	46.6	-63.0	0.74
				16469	5.518	88.3	29.0	0.65
				8631	5.517	115.9	-17.0	0.78
				12984	5.516	362.9	-247.1	3.55
				6206	5.509	866.8	-385.3	6.99
	5.72501	<12.25	14.56 ± 0.04	7377	5.728	13.2	133.0	1.41
		<12.24		7150	5.721	109.9	-178.8	2.03
		<12.24		7319	5.722	144.9	-134.2	1.72
		<12.23		6714	5.724	219.1	-45.0	1.55
		<12.23		12196	5.720	452.2	-223.4	3.85
				15831	5.726	609.3	44.1	4.12
				13611	5.727	613.8	88.7	4.23
				16565	5.733	632.6	356.0	5.68
				12674	5.719	958.5	-268.0	7.04
	5.74254	14.69 ± 0.01	14.08 ± 0.03	6949	5.746	17.1	153.8	1.63
				15869	5.746	174.3	153.8	2.00
				3116	5.747	488.0	198.2	3.75
				2766	5.748	493.7	242.7	4.03
				5740	5.739	519.6	-157.4	4.01
				16565	5.733	632.6	-424.5	6.40
	5.96731	<12.61	13.58 ± 0.28	8512	5.969	232.6	72.7	1.79
		<12.61		8941	5.968	296.3	29.7	2.09
		<12.56		9834	5.959	298.8	-357.8	4.26
		<12.61		9879	5.969	336.0	72.7	2.46
		<12.54		8588	5.956	383.7	-487.0	5.72
				30001	5.963	579.8	-185.5	4.47
				8048	5.957	740.0	-444.0	6.91
				14036	5.962	760.8	-228.1	5.80
				8861	5.961	769.1	-271.6	6.05
				5862	5.961	774.5	-271.6	6.08
				8251	5.961	930.2	-271.6	7.06
				12296	5.958	968.2	-400.9	7.92
J0100	5.33848	-	13.92 ± 0.01	9193	5.338	19.0	-22.7	0.27
				5271	5.342	373.9	166.4	2.98
				16588	5.336	717.8	-177.3	4.72
	5.51325	-	13.10 ± 0.10	5581	5.510	328.9	-149.6	2.68
				5255	5.512	420.9	-57.5	2.81
				1659	5.508	497.8	-241.7	4.15
				16252	5.514	506.2	34.5	3.32
				13791	5.510	736.4	-149.6	5.06
				17125	5.523	745.4	448.4	6.84
				11987	5.505	784.1	-380.0	6.53
	5.79746	14.10 ± 0.01	12.98 ± 0.02	-	-	-	-	-
	5.94474	13.79 ± 0.06	12.99 ± 0.04	7406	5.943	120.6	-75.1	1.14
				5394	5.941	215.8	-161.5	2.25
				6006	5.941	284.1	-161.5	2.59
				4080	5.942	309.3	-118.3	2.47
				4032	5.943	318.0	-75.1	2.34
				30	5.944	586.1	-31.9	4.08
	6.01122	<12.08	13.31 ± 0.13	6172	6.014	202.8	118.8	1.88
				14517	6.000	610.4	-480.1	6.55
				2159	6.008	759.9	-137.7	5.51
	6.11162	14.09 ± 0.08	-	-	-	-	-	-
	6.14349	14.10 ± 0.01	-	-	-	-	-	-
	6.18667	<11.97	13.95 ± 0.02	7216	6.188	83.1	55.9	0.83
		<11.96		4184	6.187	301.1	14.2	2.17
		<11.96		9273	6.187	487.1	14.2	3.50
				8514	6.182	511.4	-194.5	4.18
				17352	6.184	544.2	-111.0	4.07
				30001	6.186	552.6	-27.5	3.98
				2355	6.182	644.9	-194.5	5.04
				3783	6.183	650.7	-152.7	4.93
				9270	6.184	658.0	-111.0	4.86
				8651	6.182	698.0	-194.5	5.39
				421	6.193	702.3	264.4	5.73
				8072	6.192	760.6	222.7	5.92

Table A.1. continued.

Quasar Field	z_{abs}	log($N_{C\,II}$) cm^{-2}	log($N_{C\,IV}$) cm^{-2}	Gal ID	z_{gal}	$R_\perp$ pkpc	Δv km s^{-1}	Δr cMpc
				13753	6.180	790.5	-278.0	6.35
				15722	6.183	816.3	-152.7	6.07
				9148	6.178	822.1	-361.5	6.96
				18057	6.193	894.1	264.4	6.97
				8343	6.177	905.9	-403.2	7.70
				13073	6.175	909.0	-486.8	8.21
				6083	6.185	921.0	-69.3	6.66
				11506	6.186	921.7	-27.5	6.63
				13590	6.188	922.9	55.9	6.66
				6365	6.180	985.3	-278.0	7.62
				11400	6.182	989.1	-194.5	7.38
				15162	6.193	993.6	264.4	7.64
J159	5.73484 ± 0.00001	14.671 ± 0.012	-	-	-	-	-	-
	5.91269 ± 0.00002	14.415 ± 0.001	<12.735	9549	5.906	133.4	-290.4	3.16
			<12.741	15362	5.913	197.0	13.4	1.37
			<12.741	15408	5.913	358.8	13.4	2.48
			<12.739	12178	5.917	472.8	186.8	3.80
	5.92243 ± 0.00002	13.507 ± 0.041	-	12305	5.920	638.9	-105.3	4.56
	6.0554 ± 0.0001	14.267 ± 0.039	<12.622	7921	6.051	41.1	-199.3	2.08
	6.21904 ± 0.0001	13.423 ± 0.084	<12.715	8654	6.219	271.3	-1.8	1.96
				7617	6.208	555.2	-458.9	6.16
				17520	6.213	631.0	-251.1	5.22
				8316	6.211	821.8	-334.2	6.84
	6.2385 ± 0.0001	14.134 ± 0.024	<12.737	15962	6.239	23.4	18.4	0.25
			<12.714	9215	6.241	79.3	101.2	1.18
			<12.701	17057	6.244	81.2	225.4	2.37
			<12.774	16185	6.236	266.2	-105.9	2.21
			<12.701	16662	6.245	288.9	266.8	3.43
			<12.794	9580	6.241	429.1	101.2	3.27
			<12.759	16421	6.248	486.7	390.9	5.32
				12958	6.247	841.9	349.5	7.06
J1148[a]	6.00964 ± 0.00005	14.171 ± 0.065	-	18887	6.011	160.3	55.6	1.26
				7081	6.015	305.6	226.6	3.18
				10731	6.009	315.5	-29.9	2.23
	6.12912 ± 0.00007	13.958 ± 0.055	-	8739	6.128	307.5	-54.7	2.26
	6.19678 ± 0.00001	13.027 ± 0.072	-	11725	6.206	117.1	383.0	4.00
	6.25542 ± 0.00005	13.731 ± 0.104	-	9422	6.257	361.0	62.0	2.69
				2852	6.253	555.8	-103.3	4.17
				8234	6.256	740.2	20.7	5.37
				21959	6.250	864.4	227.3	6.68
				17433	6.256	935.0	20.7	6.79
J1120[a]	5.79539	-	13.97 ± 0.03	14866	5.792	199.0	-149.6	2.07
				7955	5.795	243.0	-17.2	1.66
	6.17111	-	13.67 ± 0.03	8334	6.168	62.3	-129.6	1.40
				6929	6.171	356.5	-4.2	2.56
				7013	6.169	374.4	-87.8	2.83
				8253	6.171	714.5	-4.2	5.12
	6.40671	13.4 ± 0.4	-	-	-	-	-	-
	6.51111	-	13.25 ± 0.06	11915	6.516	463.9	35.5	3.50
				11636	6.511	485.5	-164.0	4.00
				11300	6.514	578.9	-44.9	4.37
				10566	6.516	768.1	35.5	5.78
				1526	6.516	820.2	35.5	6.17
				12862	6.505	894.5	-403.6	7.83
				11713	6.525	920.8	394.3	7.97
				11618	6.526	946.1	434.1	8.34

Notes. The first column denote the quasar field. The second the redshift of the absorption system. The third and fourth denote the column density of C II and C IV absorption system. The fifth and sixth column denote the galaxy ID and its redshift provided by Kashino et al. (2026). The seventh column indicate the impact parameter of each galaxy. The last two column describe the line-of-sight distance for every absorber-galaxy pair as a velocity offset and the 3D comoving distance between a galaxy and an absorber. We report upper limits only for galaxies with $R_\perp \leq 500$ pkpc, used for the REW radial profile analysis.

[a] For J1148 and J1120 we do not report C IV upper limits due to the unavailable spectrum of the quasar.

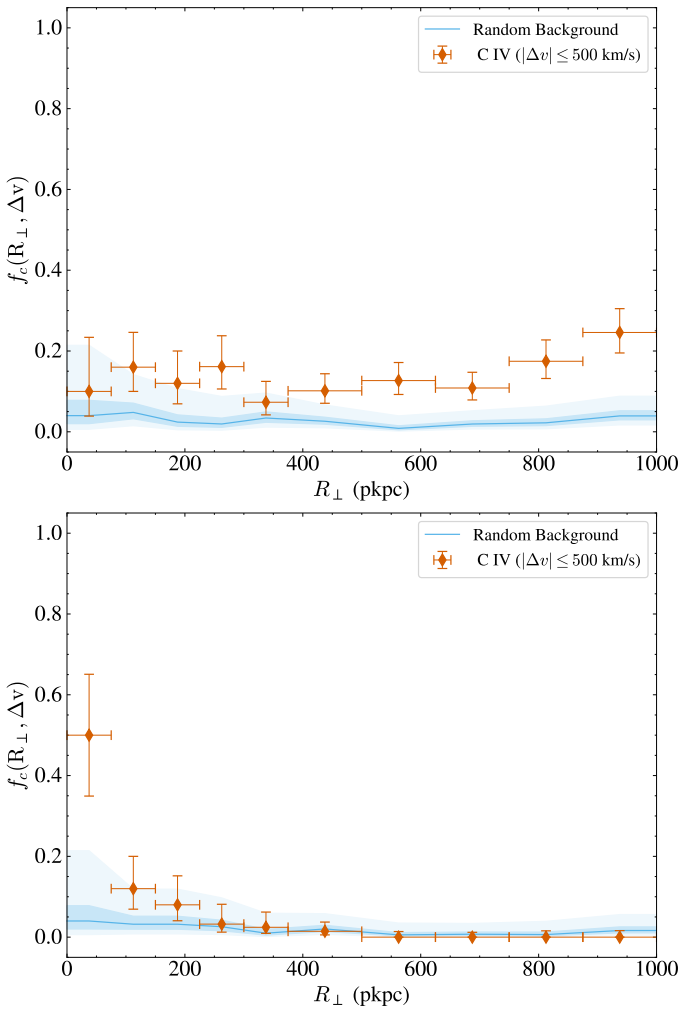

Fig. A.1. The upper panel represents the C IV covering fraction obtained excluding the systems that are also associated with low-ionization absorption lines. The lower panel represents the C IV covering fraction computed considering only the association between C IV absorbers and the closest galaxy.

Appendix B: The new X-Shooter spectrum of PSOJ159-02

In this appendix, we present the new VLT/X-Shooter observations of PSO J159-02 (0114.B-0278; PI: L. Zappacosta), which significantly improve the S/N of previous available observations (098.B-0537; PI: E. Farina). Table A.2 summarizes the observational details of the observing program. All the data were collected with a slit-width of 0.9″ for the VIS arm and 0.6″ for the NIR one. Concerning the resolution, we obtained $R = \lambda/\Delta\lambda$ of 10700 and 8100 for VIS and NIR, respectively. In particular, the NIR resolution is the nominal resolution of the arm, due to the fact that the seeing at the time of observations is larger than the slit. On the other hand, for the VIS arm, being the seeing lower than the slit, we follow the discussion in D'Odorico et al. (2023) sec. 5.2, to determine the effective resolving power, adopting

$$\mathrm{R_{eff}} = \frac{\mathrm{R_{nom}} \times \mathrm{slit}}{\mathrm{FWHM_{seeing}}} \tag{B.1}$$

and achieving a resolution of 10700. The data reduction has been performed using the open-source python software `PypeIt` (Prochaska et al. 2019, 2020), following the standard procedures for UV and NIR spectroscopic data (Schindler et al. 2020; Farina et al. 2022).

As a first step we corrected each single exposures for all the instrumental signatures (e.g., flat-field, bias). Wavelength calibration was performed using Th-Ar arc lamp exposures for the VIS arm, while for the NIR arm, the wavelength solution was derived utilizing OH sky emission lines (Rousselot et al. 2000) to ensure higher accuracy and account for instrumental flexures. Then, cosmic rays were removed through the `L.A. Cosmic` algorithm (van Dokkum 2001). For the NIR spectrum to perform sky subtraction on the 2D images difference imaging of dithered AB pairs and a 2D BSpline fitting procedure were adopted. The quasar trace was identified automatically and then extracted through optimal extraction (Horne 1986) in order to produce a 1D spectrum. Each 1D spectrum was flux-calibrated using X-Shooter standard stars. All the 1D VIS flux-calibrated spectra were then co-added on a new velocity grid, choosing a step of 10 km s^{-1}. We treated the NIR spectra similarly. As a last step, telluric absorption features were removed from the co-added and stacked spectrum using telluric grids generated by the Line-by-Line Radiative Transfer Model (`LBLRTM`) (Clough et al. 2005; Gullikson et al. 2014).

The two final spectra for the VIS and NIR arm were then stitched together following the procedure described in D'Odorico et al. (2023). We scaled the NIR spectrum to the VIS one computing, at first, the median value in the overlap region 1000-1020 μm for both arms, and then estimating the ratio of these two median. After multiplying the NIR spectrum by this scale factor, we cut the VIS reddest and NIR bluest part in order to avoid the noisiest region at 1017 nm. Finally, we performed the absolute flux-calibration scaling the final spectrum to the J-band photometry of the object, $J_{AB} = 20.00 \pm 0.10$, as reported in Bañados et al. (2016).

B.1. Fit of the continuum and rest-UV properties

To characterize the rest-frame UV-optical properties of our quasar, we used the typical procedure for fitting the spectrum of high-z quasars largely discussed in the literature (e.g., De Rosa et al. 2011; Mazzucchelli et al. 2017; Schindler et al. 2020; Bañados et al. 2021; Yang et al. 2021; Farina et al. 2022; Mazzucchelli et al. 2023; Bischetti et al. 2023). The rest-frame UV-optical spectrum of quasars is dominated by radiation from the accretion disk, which is well modeled by a power-law component. Additionally, blended high-order Balmer lines and bound-free Balmer continuum emission give rise to a Balmer pseudo-continuum, which is a non-negligible component in the considered wavelength range. Finally, there is the so-called iron pseudo-continuum. This component is mainly due to transitions of single- and double-ionized iron atoms (Fe II and Fe III), and it is particularly strong around the broad Mg II emission lines. The complete continuum model is fitted to regions that are considered free from narrow and broad emission lines, but also of absorption and telluric lines (Decarli et al. 2010; Shen et al. 2011; Mazzucchelli et al. 2017; Schindler et al. 2020; Farina et al. 2022).

Thus, we modeled the emission of the accretion disk as power-law normalized at 2500 Å. The Balmer pseudo-continuum component was modeled assuming partially optically thick gas clouds with uniform electron temperature, as discussed in Dietrich et al. (2003). Here, we fixed the normalization factor to 30% of the power-law flux at the Balmer edge (Onoue et al. 2020), and we considered an electron temperature of T_e =

Table A.2. Summary of VLT/X-Shooter observations for PSO J159-02.

X-Shooter Proposal ID	P.I.	Observation date	Exposure time (s)	# of observation
098.B-0537(A)	E.P. Farina	04 Apr 2017	1200	2
		17 Dec 2017	1200	2
0114.B-0278(A)	L. Zappacosta	25 Jan 2025	900	8
		28 Jan 2025	900	4
		29 Jan 2025	900	4
		04 Feb 2025	900	4
		05 Feb 2025	900	4

Notes. Observation log detailing the two X-Shooter programs.

15000 K, typically used in the literature (Dietrich et al. 2003; Mazzucchelli et al. 2017; Onoue et al. 2020). The iron pseudo-continuum beneath the Mg II broad emission line is modeled and fit with a template derived from the narrow-line Seyfert 1 galaxy I Zwicky-1 (Vestergaard & Wilkes 2001), linking the fitted iron Full Width Half Maximum (FWHM) to the fit of Mg II emission line. Given the coupling between the iron emission and the Mg II line, we iteratively fitted the continuum and the Mg II profile, updating the iron template parameters after each step. The procedure is repeated until the Mg II FWHM and redshift reach convergence (see also Shin et al. 2019; Schindler et al. 2020). The new full spectrum with all three components, smoothed to 20 km s^{-1} using `Astrocook`[2] (Cupani et al. 2020, 2022), is reported in Fig. B.1.

From the continuum fit we derived some of the physical properties of our quasar, starting from power-law slope to flux densities and luminosities at 1350 Åand 3000 Å. We found a power-law slope of $\alpha_\lambda = -1.19 \pm 0.02$.
Then, we followed Shen et al. (2011) to estimate the bolometric luminosity using

$$L_{bol} = 5.15 \times \lambda L_{\lambda,3000} \tag{B.2}$$

and obtaining $L_{bol} = (3.01 \pm 0.03) \times 10^{47}$ erg s^{-1}.

B.1.1. Emission lines and black hole mass

We modeled the C IV emission line as a double gaussian, while the Mg II emission line, due to its low S/N, was modeled as a single gaussian. The fits are reported in Fig. B.2.

We calculated the peak wavelength from the maximum flux value of the full-line model (all components), the FWHM, the Equivalent Width (EW), the emission line luminosity, and finally we estimated the redshift of the quasar from the line. Once these quantities are obtained, we estimated the black hole mass. Assuming virial motion of the broad-line region (BLR) clouds around a supermassive black hole, the mass can be inferred from the virial theorem, which relates the gas velocity dispersion, traced by the FWHM of the broad emission line (FWHM$_{\rm BLR}$), to the gravitational potential of the black hole $M_{\rm BH}$ as

$$\mathrm{M_{BH}} = f \cdot \frac{\mathrm{R_{BLR}} \cdot \mathrm{FWHM^2_{BLR}}}{G} \tag{B.3}$$

where $\mathrm{R_{BLR}}$ indicates the radius from the SMBH to the emission line, and f is a factor that takes into account our poor knowledge about orientation, geometry and kinematics of the BLR. Thus, to derive the black hole mass we used the so-called single-epoch virial relation provided by Vestergaard & Peterson (2006) for the C IV emission line, and Vestergaard & Osmer (2009) for the Mg II emission line. These are expressed as

$$\mathrm{M_{BH,Mg\,II}} = 10^{6.86}\left[\frac{\mathrm{FWHM_{Mg\,II}}}{10^3\ \mathrm{km\ s^{-1}}}\right]^2\left[\frac{\lambda L_\lambda(3000\text{Å})}{10^{44}\ \mathrm{erg\ s^{-1}}}\right]^{0.5} M_\odot \tag{B.4}$$

where $\lambda L_\lambda(3000\text{Å})$ is the monochromatic luminosity at 3000 Å rest-frame wavelength, and

$$\mathrm{M_{BH,C\,IV}} = 10^{6.66}\left[\frac{\mathrm{FWHM_{C\,IV,}\mathit{corr}}}{10^3\ \mathrm{km\ s^{-1}}}\right]^2\left[\frac{\lambda L_\lambda(1350\text{Å})}{10^{44}\ \mathrm{erg\ s^{-1}}}\right]^{0.53} M_\odot \tag{B.5}$$

where $\lambda L_\lambda(1350\text{Å})$ is the monochromatic luminosity at 1350 Å rest-frame wavelength. Here, we adopted the outflow-corrected FWHM to account for the strong wind component affecting the C IV emission line (Mazzucchelli et al. 2023). So, the expression for the corrected FWHM is taken from Coatman et al. (2017):

$$\mathrm{FWHM_{C\,IV\,corr}} = \frac{\mathrm{FWHM_{C\,IV}}}{0.36 \times \frac{\mathrm{C\,IV\ blueshift}}{10^3\ \mathrm{km\ s^{-1}}} + 0.61} \tag{B.6}$$

where C IV blueshift is the velocity difference between the C IV centroid and the quasars' systemic redshifts, obtained from [C II] emission line (Decarli et al. 2018). Here the C IV blueshift corresponds to 1649 km s^{-1}.
From the black hole mass measurements, we estimated the Eddington luminosity as

$$L_{\mathrm{Edd,C\,IV/Mg\,II}} = 1.3 \times 10^{38}\left(\frac{M_{\mathrm{BH,C\,IV/Mg\,II}}}{M_\odot}\right)\ \mathrm{erg\ s^{-1}} \tag{B.7}$$

and consequently the Eddington ratio as

$$\lambda_{\mathrm{Edd,C\,IV/Mg\,II}} = \frac{L_{\rm bol}}{L_{\mathrm{Edd,C\,IV/Mg\,II}}}. \tag{B.8}$$

All these quantities, derived from the C IV and Mg II emission lines, are finally summarized in Table B.1.

Appendix C: PSO J159-02 absorption systems

In this appendix, we present the five absorption systems found in PSO J159-02. The identified ionic transitions are O I λ 1302 Å, C II $\lambda\lambda$ 1334, 1335 Å, Si II $\lambda\lambda\lambda$ 1260, 1304, 1526 Å, Fe II $\lambda\lambda\lambda\lambda\lambda\lambda$, 1608, 2344, 2374, 2382, 2586, 2600 Å, Al II λ 1670 Å, Mg II $\lambda\lambda$ 2796, 2803 Å. All absorption lines were fitted with Voigt profiles using the analysis software `Astrocook` (Cupani et al. 2020, 2022). The results of the fit are reported in Table C.1.

[2] https://das-oats.github.io/astrocook/

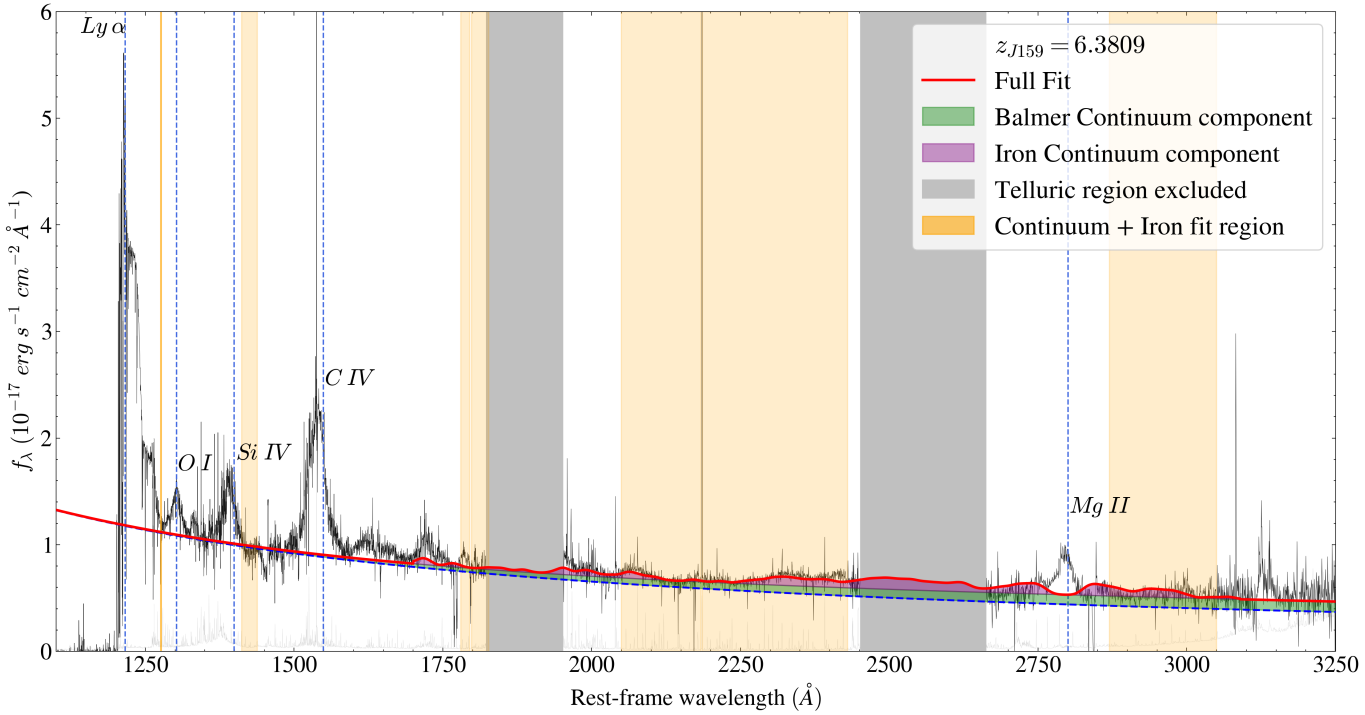

Fig. B.1. Best fit to the PSO J159-02 X-Shooter spectrum. The spectrum, smoothed to 20 km s^{-1}, is depicted in black, with flux errors in gray. The dashed orange vertical bars indicate the wavelengths used for the fit of the continuum, being very careful to avoid spikes. The dashed gray vertical bars indicate the wavelength regions in which there are strong telluric residuals after the telluric correction. The red line denotes the combined fit of the continuum, where the blue dotted line indicates the power-law component, the green shaded area indicates the Balmer continuum contribution, and the shaded magenta area denotes the iron continuum contribution.

Table B.1. Emission lines and quasar properties.

	z	FWHM^a km s^{-1}	EW Å	$\log(M_{\rm BH}/M_\odot)$	$\log(L_{\rm Edd}/10^{47}{\rm erg\ s^{-1}})$	$\lambda_{\rm Edd}$
C IV	6.3403 ± 0.0004	6104 ± 290	52.33 ± 1.22	9.53 ± 0.04	4.08 ± 0.04	0.74 ± 0.06
Mg II	6.3685 ± 0.0002	2908 ± 146	21.17 ± 2.12	9.51 ± 0.05	4.24 ± 0.06	0.71 ± 0.05

Notes. ^{a}: We report the C IV FWHM not corrected from the outflow.

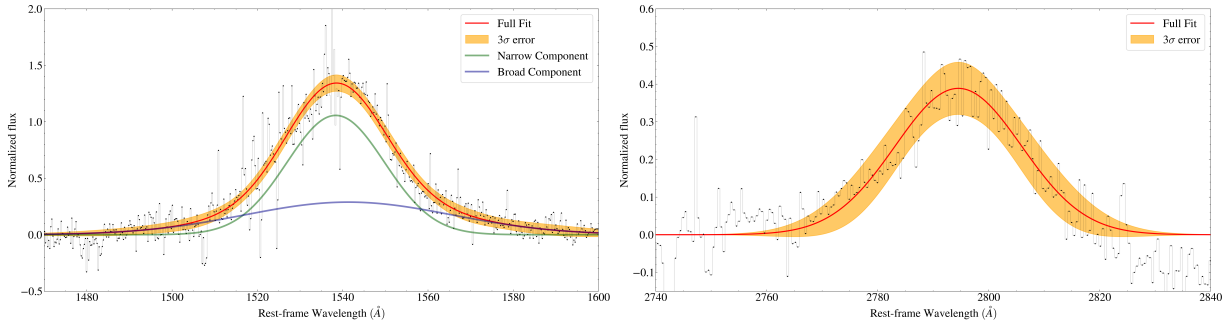

Fig. B.2. Best-fit model of the C IV emission line (left-hand panel) and Mg II emission line (right-hand panel) in the rest-frame spectrum, rebinned to 50 km s^{-1}. The black points denotes the observed spectrum after subtracting continuum, while the red curve represents the total model given by double gaussian component. The green and blue curve denote the narrow and broad components, respectively. The orange shaded region marks the 3σ uncertainty on the fit.

Table C.1. Voigt profile fit results for the absorption systems identified towards PSO J159-02.

Ion	z_{comp}	b km s^{-1}	log N (cm^{-2})
	z_{abs} = 5.73484		
C II 1334	5.73316 ± 0.00001	6.00	13.266 ± 0.023
	5.73491 ± 0.00001	24.45 ± 0.32	14.642 ± 0.012
C II* 1335[a]	5.73491	6.00	13.669 ± 0.021
Si II 1526[a]	5.73491	27.73 ± 2.49	14.195 ± 0.034
Fe II 2600[a]	5.73491	9.00	14.261 ± 0.020
Fe II 1608[a,b]	5.73491	9.00	14.261
Fe II 2344[a,b]	5.73491	9.00	14.261
Fe II 2374[a,b]	5.73491	9.00	14.261
Fe II 2382[a,b]	5.73491	9.00	14.261
Fe II 2586[a,b]	5.73491	9.00	14.261
Al II 1670[a]	5.73491	9.00	13.400 ± 0.075
Mg II 2796[a]	5.73491	9.00	15.461 ± 0.137
Mg II 2803[a]	5.73491	9.00	15.461
	z_{abs} = 5.91269		
O I 1302	5.91166 ± 0.00002	6.00	13.552 ± 0.036
	5.91308 ± 0.00001	39.08 ± 0.47	14.410 ± 0.008
	5.9154 ± 0.0001	6.00	13.284 ± 0.093
Si II 1304[d]	5.91166	6.00	13.142 ± 0.046
	5.91308	32.87 ± 0.17	13.656 ± 0.016
Si II 1526[d]	5.91308	32.87	13.656
C II 1334[d]	5.91166	16.13 ± 0.30	13.904 ± 0.021
	5.91308	29.78 ± 0.45	14.265 ± 0.012
Fe II 2374[d]	5.91308	15.00	13.023 ± 0.024
Fe II 1608[c,d]	5.91308	15.00	13.023
Fe II 2344[c,d]	5.91308	15.00	13.023
Fe II 2382[c,d]	5.91308	15.00	13.023
Fe II 2600[c,d]	5.91308	15.00	13.023
	z_{abs} = 5.92243		
C II 1334	5.92315	38.52 ± 5.47	13.347 ± 0.050
Si II 1304[a]	5.92168 ± 0.00007	13.06 ± 5.27	12.982 ± 0.098
	5.92315 ± 0.00006	9.00	12.976 ± 0.062
	z_{abs} = 6.0554		
O I 1302	6.05445 ± 0.00001	18.65 ± 0.79	14.434 ± 0.011
	6.05623 ± 0.00003	6.00	13.300 ± 0.087
Si II 1304[d]	6.05445	21.39 ± 5.76	13.223 ± 0.063
C II 1334[d]	6.05445	32.97 ± 3.64	13.948 ± 0.037
	6.05623	40.36 ± 3.38	14.016 ± 0.029
Mg II 2796[d]	6.05445	9.00	12.574 ± 0.131
	6.05520 ± 0.00004	9.00	13.187 ± 0.078
	6.05623	9.00	13.145 ± 0.087
Mg II 2803[d]	6.05445	9.00	12.574
	6.05520	9.00	13.187
	6.05623	9.00	13.145
	z_{abs} = 6.21904		
C II 1334	6.21829 ± 0.00018	19.94 ± 13.46	12.998 ± 0.152
	6.21977	26.11 ± 9.62	13.219 ± 0.098
Si II 1260[a]	6.21977 ± 0.00002	14.11 ± 1.83	12.357 ± 0.019
	z_{abs} = 6.2385		
C II 1334	6.23695	21.15 ± 3.35	13.836 ± 0.031
	6.24017 ± 0.00009	47.16 ± 4.86	13.829 ± 0.036
Si II 1260[a]	6.23695 ± 0.00001	21.42 ± 0.84	12.865 ± 0.010
	6.23951 ± 0.00002	45.02 ± 1.57	12.822 ± 0.011
Mg II 2796[a]	6.23695	9.00	12.895 ± 0.059
	6.23951	9.00	13.048 ± 0.052
Mg II 2803[a]	6.23695	9.00	12.895
	6.23951	9.00	13.048

Notes. List of the individual kinematic components fitted for each ionic transition. Values without explicit errors are tied to other components during the fitting process. For those components for which the b values go below the specific X-Shooter arm resolution, we set their values to the minimum possible: 6.00 and 9.00 for the VIS and NIR arms, respectively.
[a] The z-values for this component were tied to those for C II.
[b] The b- and log(N)-values for this component were tied to those for Fe II 2600.
[c] The b- and log(N)-values for this component were tied to those for Fe II 2374.
[d] The z-values for this component were tied to those for O I.

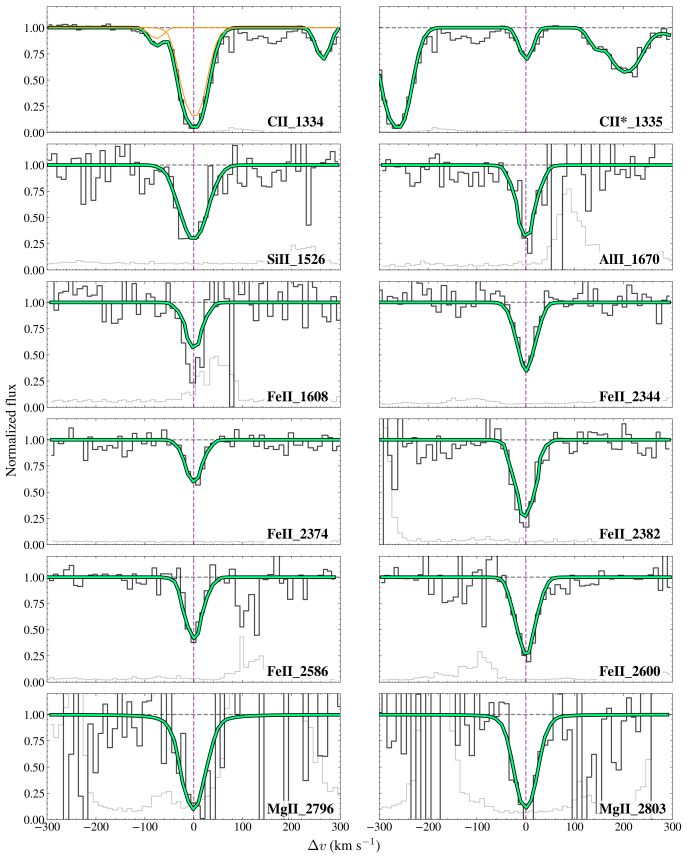

Fig. C.1. Voigt profile fits of absorption system at z = 5.73484 found in J159 quasar spectrum. The flux is denoted in black, the error in gray, and full Voigt profile in green. The individual Voigt component fits are shown in orange.

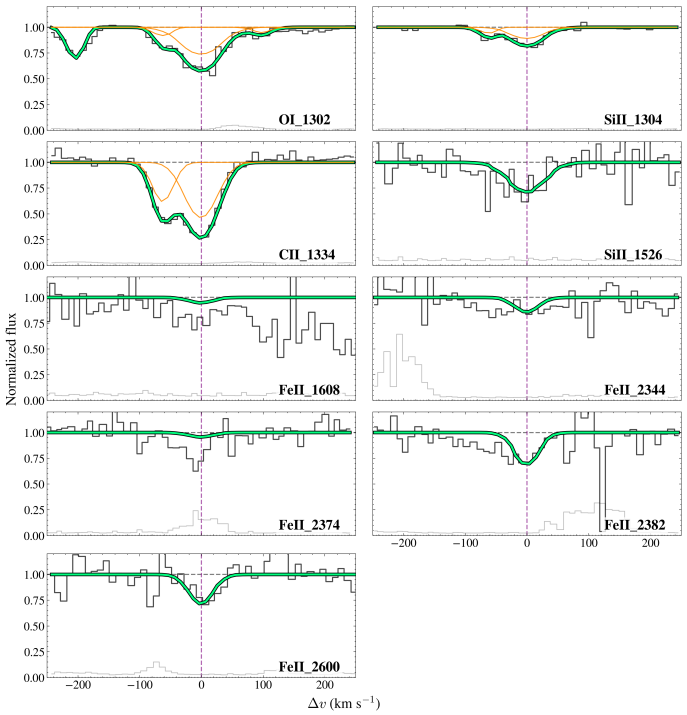

Fig. C.2. Voigt profile fits of absorption system at z = 5.91269 found in J159 quasar spectrum.

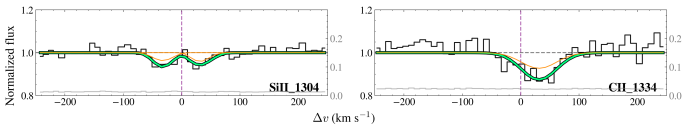

Fig. C.3. Voigt profile fits of absorption system at $z = 5.92243$ found in J159 quasar spectrum.

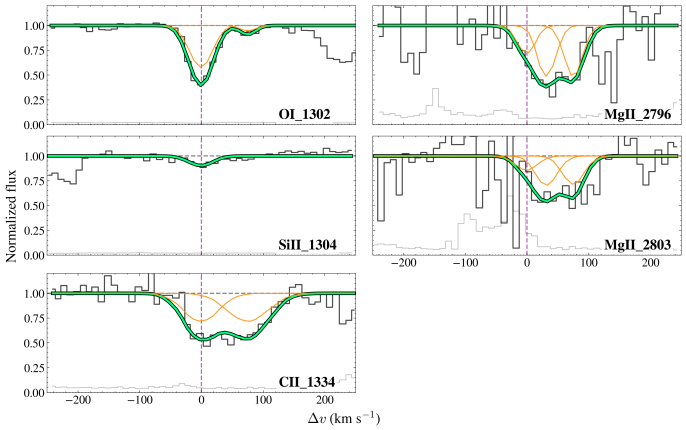

Fig. C.4. Voigt profile fits of absorption system at $z = 6.0554$ found in J159 quasar spectrum.

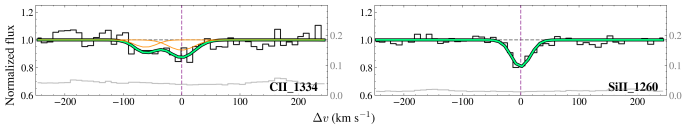

Fig. C.5. Voigt profile fits of absorption system at $z = 6.21904$ found in J159 quasar spectrum.

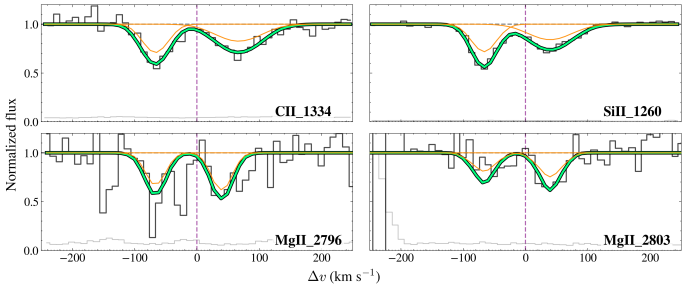

Fig. C.6. Voigt profile fits of absorption system at $z = 6.2385$ found in J159 quasar spectrum.